University of Aveiro

2014

Department of Materials and Ceramic Engineering

Marco Pinheiro de Oliveira

Corrosion inhibition study on Fe-Zn and AA2024-CFRP galvanic couples.

University of Aveiro Department of Materials and Ceramic Engineering

2014

Marco Pinheiro de Oliveira

Corrosion inhibition study on Fe-Zn and AA2024-CFRP galvanic couples.

Dissertation submitted to the University of Aveiro to fulfill the requirements for obtaining a Master's degree in materials engineering, held under the scientific guidance of Dr. Silvar Kallip, assistant researcher at the Department of Ceramic and Materials Engineering at the University of Aveiro and Dr. Mikhail Zhelukedvich invited professor in the Department of Ceramic and Materials Engineering at the University of Aveiro.

The jury

president

Prof. Dr. Mário Guerreiro Silva Ferreira,
Full Professor, Universidade de Aveiro
Prof. Dr. João Carlos Salvador Santos Fernandes,
Full Professor, Instituto Superior Técnico - Universidade Técnica de Lisboa
Dr. Silvar Kallip,
Equivalent to Assistant Researcher, Universidade de Aveiro

Acknowledgements

A huge thank you to the University of Aveiro and Airbus group for having given me the opportunity to intern at one of the world's largest companies, especially to Dr. Mikhail Zhelukedvich and Mr. Theodor Hack for putting their trust in me.
Thanks to my advisor Dr. Silvar Kallip for everything he taught me and all the help he gave me.
A thanks to Sonja Nixon and all my colleagues at Airbus group for all support and patience to explain and help when needed.
I am also grateful to my laboratory colleagues at the University of Aveiro.
A big thank you to my family and friends for all the support they gave me, especially to Daniel Vieira and Alexandre Rocha.
The EU FP7 project PIAPP-GA-2013-612415 (PROAIR) and FCT Exploratory project IF/00856/2013/CP1162/CT0019 are greatly acknowledged for financial support.

Palavras chave

Par galvanico, corrosão, inibição, AA2024, CFRP, Ferro, Zinco, Sinergia

Resumo

Embora pares galvanicos de Zn e Fe sejam industrialmente comuns, os de AA2024 e CFRP são utilizados hoje em dia principalmente na indústria aeronáutica, devido à sua baixa densidade e boas propriedades mecânicas. É também evidente que os problemas de corrosão surgem quando estes materiais estão galvanicamente acoplados e a corrosão do material estrutural menos nobre ocorre. Medidas atuais para a proteção do AA2024, especialmente quando ativado galvanicamente, são ineficientes ou caras. Portanto, estratégias de proteção novas estão em desenvolvimento com uma demanda industrial significativa.

O principal objetivo deste trabalho foi o de procurar e desenvolver novas estratégias de inibição de corrosão para sistemas de materiais diferentes industrialmente relevantes, onde ocorrem pares galvânicos, tais como Zn + Fe e AA2024 + CFRP. A selecção de inibidores utilizada, contem sistemas de inibidores individuais, bem como algumas misturas potencialmente sinérgéticas. Foi demonstrado que a corrosão em sistemas galvânicos especificos, pode ser inibida com sucesso, usando combinações especialmente concebidas de inibidores de corrosão dedicados com base na cooperação sinérgica dos seus diferentes mecanismos de inibição da corrosão.

Uma gama de técnicas eletroquímicas, como EIS e ZRA juntamente com a completa análise e modelação de dados, foram usadas sistematicamente, a fim de avaliar as propriedades de corrosão para todas as circunstâncias selecionadas.

keywords

Galvanic couple, corrosion, inhibition, AA2024, CFRP, Iron, Zinc, Synergy

abstract

While the galvanic joints of Zn and Fe are industrially widespread, the AA2024 and CFRP are widely used together nowadays mostly in aeronautical industry due to their light weight and good mechanical properties. It is also clear that the corrosion problems arise when these materials are galvanically coupled and the corrosion of less noble structural material occurs. Current measures for the protection of the AA2024, especially when galvanically activated, are inefficient or expensive. Therefore novel protection strategies are under development with a significant industrial demand.

The main objective of this work was to seek and design new corrosion inhibition strategies for industrially relevant dissimilar material systems where the galvanic combinations occur, such as Zn + Fe and AA2024 + CFRP. The selection of inhibitors contained the single inhibitor systems as well as some dedicated potentially synergistic mixtures. It has found that the corrosion impact on specific galvanic systems can be successfully inhibited by using specially designed and dedicated combinations of corrosion inhibitors based on the synergistic cooperation of their different corrosion inhibition mechanisms.

A range of electrochemical techniques such as EIS and ZRA together with a full analysis and modelling of data were systematically used in order to evaluate the corrosion properties for all selected circumstances.

Stichworte

Galvanisches Element, Korrosion, Hemmung, AA2024, CFK, Eisen, Zink, Synergy

abstrakt

Galvanische Verbindungen aus Fe und Zn finden in einem breiten Anwendungsspektrum industriellen Einsatz. Demgegenüber werden Paarungen aus AA2024 und CFK aufgrund ihrer geringen Dichte und der guten mechanischen Eigenschaften derzeit hauptsächlich in der Luft- und Raumfahrt eingesetzt. Das elektrochemische Gefälle zwischen beiden Werkstoffen führt zu einer ausgeprägten Korrosionsproblematik, wobei der unedlere Strukturwerkstoff angegriffen wird. Herkömmliche technische Maßnahmen zum Schutz des AA2024 vor Korrosion, insbesondere in elektrisch leitfähigen Umgebungen, sind leider entweder ineffizient oder aber zu kostenintensiv. Die enorme Nachfrage von Seiten der Industrie führt dazu, dass aktuell verstärkt an alternativen Korrosionsschutz-Strategien geforscht wird.

Das Hauptziel dieser Arbeit bestand darin, neue Korrosionsinhibitions-Strategien aufzuzeigen und zu untersuchen, um zukünftig auch den industriellen Einsatz galvanisch heikler Paarungen etwa aus Zn und Fe oder aus AA2024 und CFK zu fördern. Bei der Auswahl der Inhibitoren wurden sowohl einzelne Inhibitorsysteme als auch ausgesuchte potentiell synergetische Mischungen berücksichtigt. Es wurde herausgefunden, dass das Korrosionsrisiko spezifischer galvanischer Werkstoffpaarungen mittels geeigneter Inhibitoren erfolgreich gemindert werden konnte. Dazu wurden spezielle Kombinationen aus Inhibitorsystemen verwendet, deren Inhibitionsmechanismen sich untereinander synergetisch ergänzten.

Mit Hilfe einer große Bandbreite an elektrochemischen Untersuchungsmethoden wie EIS und ZRA sowie einer fundierten Datenanalyse und Modellierung konnte das jeweilige Korrosionsverhalten für alle untersuchten Umgebungsbedingungen eingehend untersucht und bewertet werden.

Index

Index of figures

Index of tables

Index of abbreviations

|Z| ..... *Total impedance*
AA2024 ..... *Aluminium alloy 2024*
AC ..... *Alternated current*
AP ..... *Artificial Polarization*
BIA ..... *Benzimidazole*
BTA ..... *Benzotriazole*
CFRP ..... *Carbon Fiber Reinforced Plastic*
EIS ..... *Electrochemical Impedance Spectroscopy*
GC ..... *Galvanic Couple*
Re ..... *Rare Earth*
RMS ..... *Root Mean Square*
Rpol ..... *Polarization Resistance*
SCE ..... *Saturated Calomel Electrode*
SVET ..... *Scanning Vibrating Electrode Technique*
ZRA ..... *Zero Resistance Ammeter*

Index of Units

Unit Symbol	Unit Name	Quantity Name
A	Ampere	Electric current
Hz	Hertz	Frequency
kg	Kilogram	Mass
m	Meter	Length
mol	Mole	Amount of substance
N	Newton	Force, Weight
Ω	Ohm	Electric resistance, Impedance
Pa	Pascal	Pressure
s	Second	Time
S	Siemens	Electrical conductance
V	Volt	Electrical potential difference

1. Introduction

1.1. Objectives and Motivation

The main objective of this work is to seek and design new corrosion inhibition strategies for industrially relevant dissimilar material systems where the galvanic combination occurs, such as Zn + Fe and AA2024 + CFRP.

While the galvanic joints of Zn and Fe are industrially widespread, the AA2024 and CFRP are used together nowadays mostly in aeronautical industry, due to their light weight and good mechanical properties. It is also obvious that the corrosion problems arise when these materials are galvanically coupled and the corrosion of less noble structure material occurs. Current measures for the protection of the AA2024, especially when galvanically activated, are inefficient or expensive. Therefore novel protection strategies are under development with a significant industrial demand.

For this reason novel experimental methodologies, for corrosion testing of galvanically coupled materials, have to be devised and improved. During this work, advances in corrosion testing of galvanically coupled materials are also to be achieved.

1.2. Galvanic corrosion

Galvanic corrosion occurs when two different phases are electrically linked, one material will act as an anode while the nobler as a cathode, greatly accelerating the corrosion process (Figure 1 b).

The SVET image shows that in the galvanically linked dissimilar materials the ionic currents and so the corrosion are more than one order of magnitude higher than on the single electrodes (Figure 1 a).

When in contact with an electrolyte, electrical current flows from the anode to the cathode. This causes the degradation of the anode material, as it is consumed when dissolved and providing electrons for the cathodic reactions.

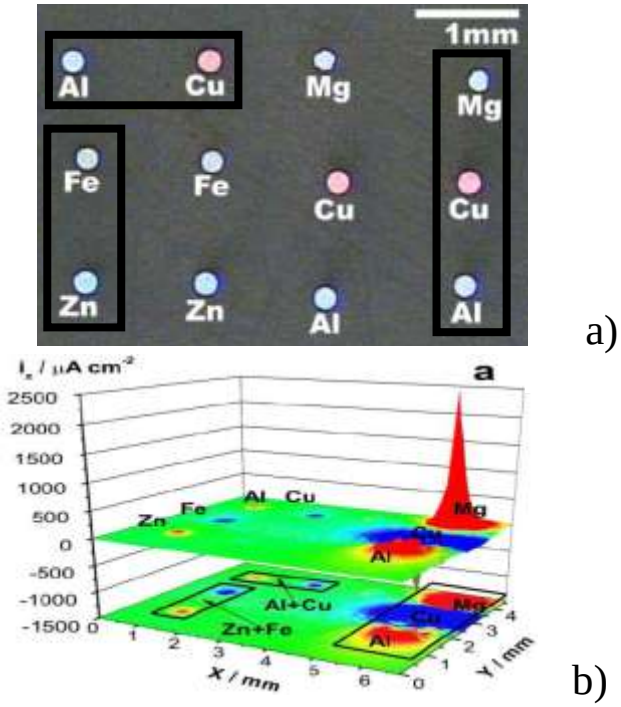

Figure 1. Multi-electrode cell with both single and coupled electrodes a) location of the electrodes and scheme of the linking, b) SVET measurement in a corrosive medium of 0,05 M NaCl [1].

In an aqueous medium the simplified electrochemical reactions involved in corrosion are as presented in reaction (1) for the anode, in which M is the metal suffering oxidation and n is the number of electrons involved in the reaction. For the cathode side the common reactions are (2) and (3):

$$M \rightarrow M^{n+} + ne^- \quad (1)$$

In acid mediums, the reduction of water:

$$2H^+ + 2e^- \rightarrow H_2 \quad (2)$$

In neutral or basic mediums, the reduction of oxygen:

$$O_2 + 2H_2O + 4e^- \rightarrow 4OH^- \quad (3)$$

Galvanic corrosion is critical for mechanical properties for multi material structures. It is more intensive on the interface of the junctions of different materials, compromising the mechanical integrity of the junctions.

Common ways to prevent galvanic corrosion is to either create an electrical barrier between the materials, or to create a barrier to prevent the surface exposure to corrosive mediums.

1.3. Galvanic corrosion in AA2024 – CFRP couple

On the AA2024-CFRP pair the corrosion processes takes place on the aluminium substrate. Corrosion of the cathode material or other surface reactions are negligible, as long as the polymer used does not degrade in high pH values or in the presence of other aggressive species ions.

Figure 2 a) shows a simplified scheme of the mechanisms involved in galvanic corrosion on the AA2024-CFRP couple.

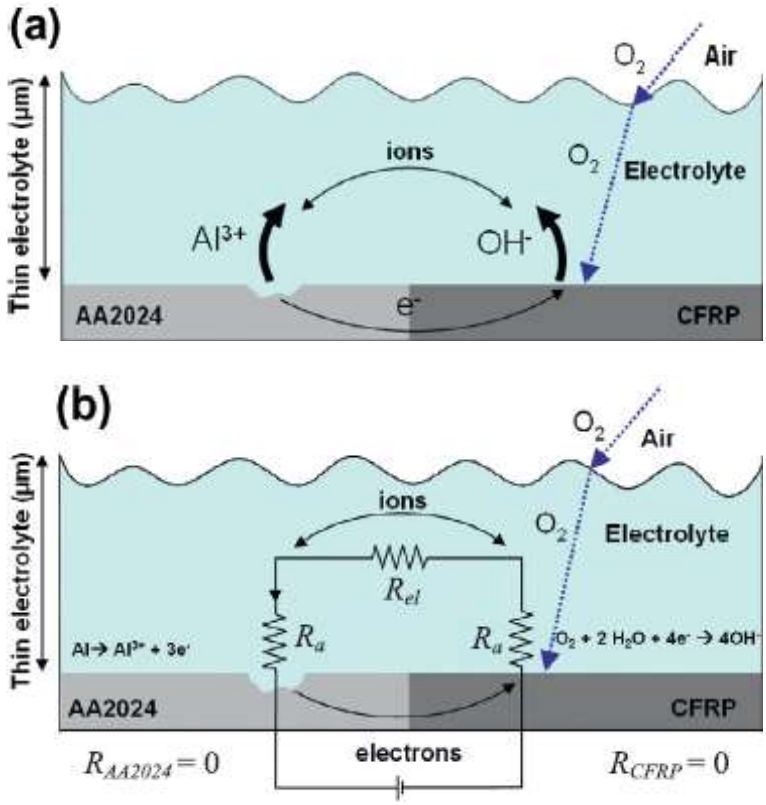

Figure 2. a) simplified corrosion mechanisms and b) simplified electrical circuit model for AA2024-CFRP galvanic corrosion [2]

Figure 2 b) shows the locations of the simplified anodic and cathodic reactions and electrical equivalent circuit associated with this process.

In the galvanic series presented in Figure 3, one can see that graphite is a very noble material when compared with Al alloys. The electrochemically active sites in CFRP are the carbon fiber surfaces and they behave as graphite. This is the underlying cause and very strong driving force of the corrosion processes that occur in the galvanic joints.

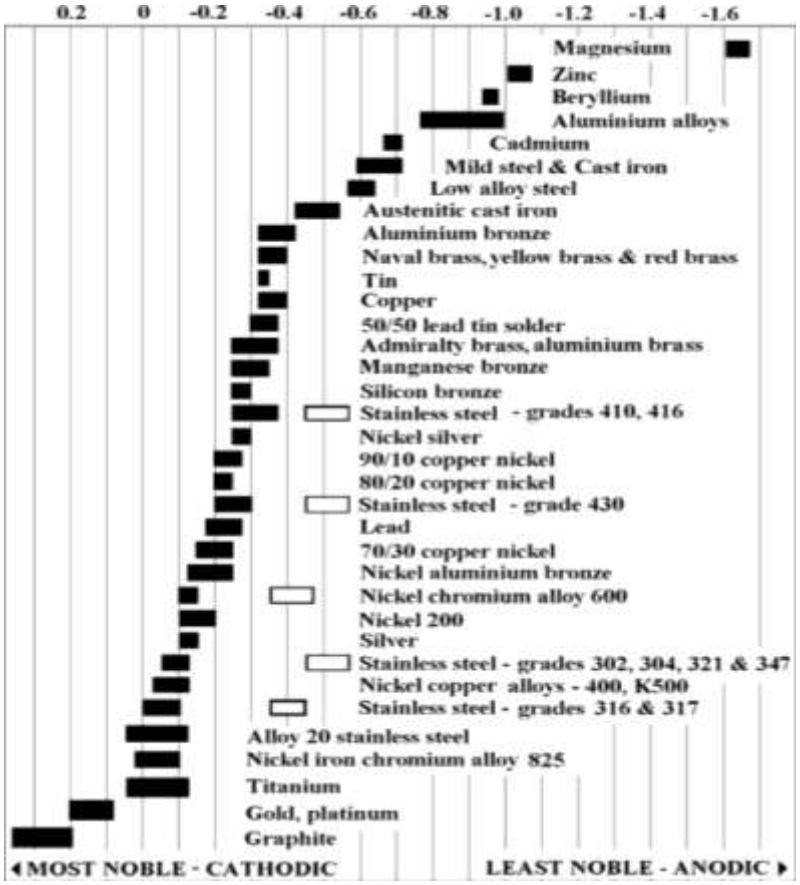

Figure 3. Galvanic series for flowing sea water vs. SCE [3]

1.4. Galvanic corrosion in Fe-Zn

Zinc - iron combination in galvanic contact are very common in the industry, although not so common as pure metals, but in galvanized steel components or galvanized steel fixed with steel rivets or bolts. This is particularly dangerous, seeing as these couplings degrade the zinc coating, faster than would be expected by spontaneous corrosion.

This can be seen in Figure 4 c) where the SVET map shows clearly that in the case of galvanically coupled systems the ionic currents above the cathode and anode, which result from corrosion processes, are orders of magnitude higher than the non-coupled systems, which are not even visible given the current range.

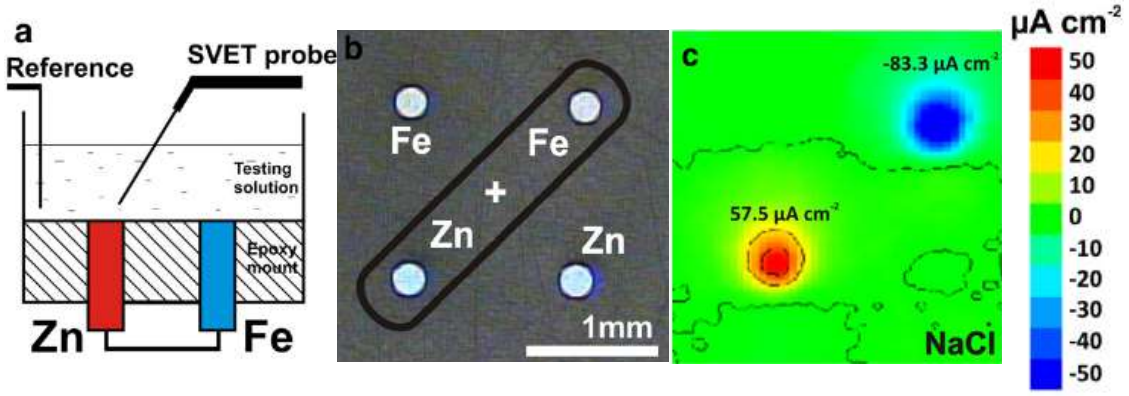

Figure 4. " Diagram of SVET microelectrode cell concept for Zn+Fe galvanic system (a), microphotograph of the galvanic cell configuration (b) and obtained SVET maps taken after 2 h of immersion in different inhibitor solutions with Fe and Zn electrodes electrically coupled in 0.05 M NaCl (c)"[4].

These processes are aggravated when in thin film conditions, like watery films formed by condensation or presence of dew. This means that as oxygen dissolves from the air in to de electrolyte, it has a smaller distance to reach the cathode. So, the thinner the film is, the higher is the oxygen availability near to the cathode substrate.

Figure 5 shows that most of the ionic currents happen under 1mm of electrolyte. Further demonstrating, that thin film environments pose no difficulty to corrosion processes. It is also visible that the morphology of the current profile at anodic site has one clear peak while in the cathodic site it seems to be more spread.

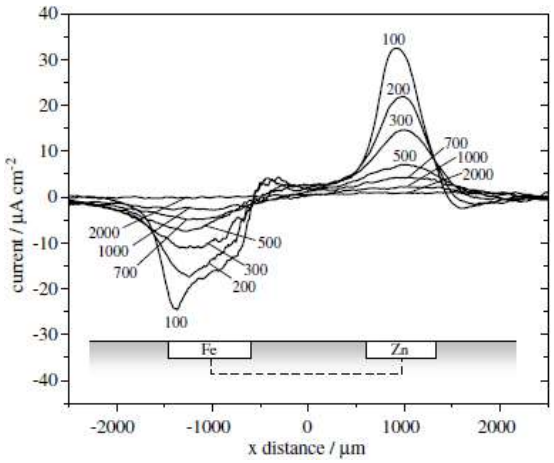

Figure 5. "Ionic current lines obtained at different distances (indicated in µm) above the galvanic couple immersed in 0.1M NaCl."[5]

1.5. Materials

1.5.1. Iron

Iron has a relatively straight forward corrosion mechanism in Cl^- rich mediums at neutral pH. Iron oxidation follows reaction (1) in which *M* is Fe and *n* is (2) and the reduction of oxygen follows reaction (3).

These reactions give rise to ion currents in the solution that can be measured using SVET. In Figure 6 a the results from SVET measurements show the time evolution of spontaneous iron corrosion and how the anodic and cathodic parts of the substrate are clearly separated and change over the time while the anodic reaction covers the metal substrate with corrosion products.

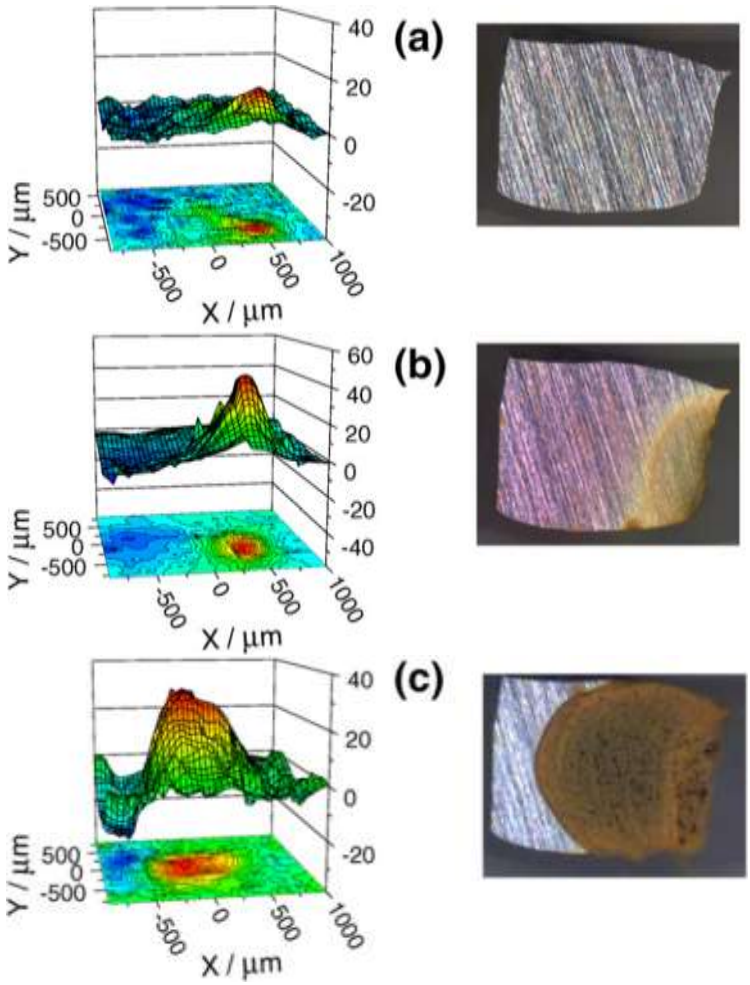

Figure 6. "Ionic current mapping (left) and video images (right) of a pure iron electrode during immersion in 0.1 M NaCl at selected exposure times: (a) ca. 5 min, (b) 1 h, and (c) 1 day. Electrode size: ≈1 x 1 mm^2. Current scales are given in µA cm^{-2}." [5]

1.5.2. Zinc

Zinc has a similar corrosion mechanisms as iron. It follows the reaction (1) in which *M* is Zn and *n* is (2). In neutral pH and in a Cl^- rich medium the cathodic reaction is also the reduction of the dissolved O_2 following reaction (3).

The anodic and cathodic sites can be monitored by measuring the anodic and cathodic currents using SVET, as can be seen in Figure 7. The anodic and cathodic sites are localized, with the anodic zone forming a pit with very high anodic currents after one day and with a cathodic zone initially localized near the anodic zone and after a day more spread out over the surface area as the original cathodic site got covered with corrosion products.

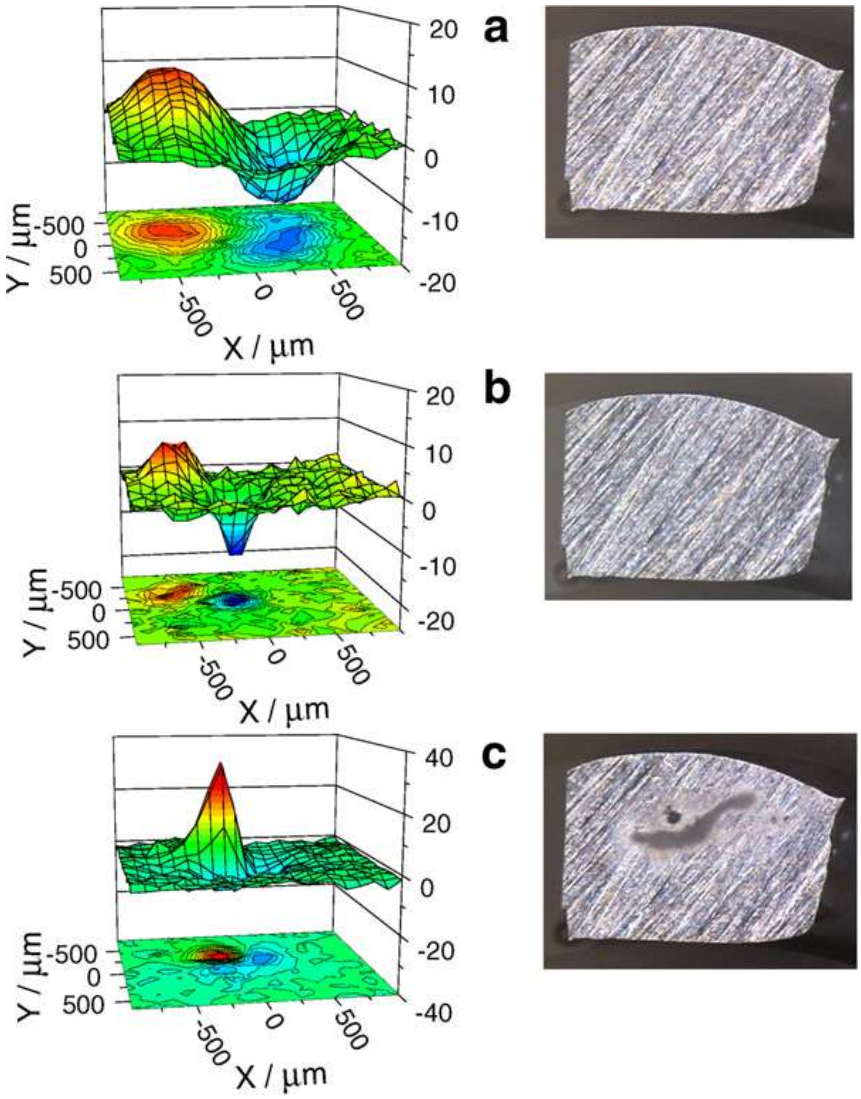

Figure 7. "Ionic current mapping (left) and video images (right) of a pure zinc electrode during immersion in 0.1 M NaCl at selected exposure times: (a) ca. 5 min, (b) 1 h, and (c) 1 day. Electrode size: ≈1 x 1 mm^2. Current scales are given in µA cm^{-2}." [5]

1.5.3. Aluminium alloy 2024-T351

The AA2024-T351 aluminium alloy is a widely used material in the aeronautical industry. It combines good mechanical properties with corrosion resistance (with respect to magnesium alloys) and light weight for a reasonable price. For that reason it is used in the fuselage and structural part of the plane [6]. As a loss in properties in these crucial sectors would be catastrophic, therefore high reliability must be provided in the long term properties of the alloy.

The 2xxx series is the designation for Cu addition as an alloying agent, the 2024 has also a small addition of Mg. The Cu is added to raise the metal strength and the Mg accelerates precipitation, rising hardness [6]. These compounds form an intermetallic phase (Al_2MgCu) in the Al alloy matrix which plays an important role in localized self-galvanic corrosion [7].

Even though the aluminium surface is usually protected by a naturally insoluble oxide film [8], the presence of Cl^- in the environment can cause pitting attack, which compromises the mechanical properties. When galvanically coupled, this process will be drastically accelerated [9]. The simplified pitting mechanism can be seen in Figure 8.

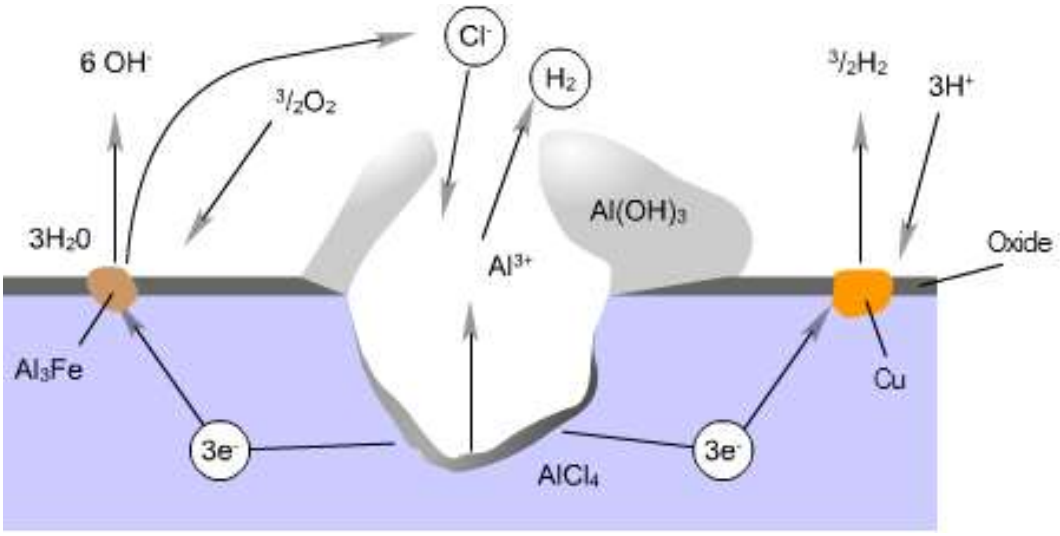

Figure 8. Simplified illustration of AA2024 pitting and role carried by precipitates [9].

1.5.4. CFRP

In recent years there has been a high demand for higher efficiency and lower carbon emissions in aeronautical industry. For this reason, low weight and good mechanical properties have been key features for proposed materials. The reason is that lower weight and less material usage have high impact in fuel consumption and overall price of an aircraft (10).

For that reason CFRP has been in the spot light as a material to substitute many structural components. In a comparison with AA2024, the density of CFRP is 1,82 g/cm^3 and of AA2024 is 2,78 g/cm^3 and the ultimate tensile strengths are 1440 MPa and 470 MPa for CFRP and AA2024 respectively. One can see that in terms of specific strength CFRP has about 800 kN.m/kg and aluminium has about 170 kN.m/kg. So it is no wonder, the use of CFRP is becoming more and more common, from sports cars to aviation and space industry.

Electrochemically it behaves as graphite. It is a noble material, as seen in Figure 3, so as soon as there is an electrical connection with less noble materials it acts as an active cathode promoting galvanic corrosion.

1.6. Inhibitors

1.6.1. Na_2WO_4 and Na_2MoO_4

Unlike chromate the tungstate is not a good oxidizer, but like chromate the solutions of tungstate and molybdate condense to give the isopolytungstates and isopolymolybdates upon acidification[11] [12].

These form when the anodic currents cause a slight fall in pH, between 6 and 4. As they are insoluble and cover the anodic areas, they are successfully preventing further corrosion.

1.6.2. $NaVO_3$

Vanadate's are thought to be cathodic inhibitors forming barriers over the noble materials and acting as a barrier that to prevents oxygen reduction[13] .

It has been found to be a good inhibitor for corrosion in AA2024 T3, by blocking the intermetallic phases. But this often happens with slow kinetics of barrier formation, taking up to 35min to develop a first monolayer over the substrate [14].

1.6.3. $K_2Cr_2O_7$

The inhibiting power of the chromate inhibitor, is due to its strong oxidizing capability and it reduces rapidly from Cr(VI) to Cr(III) according to reaction (4) [15].

$$2CrO_2^{4-} + 5H_2O + 6e^- = Cr_2O_3 + 10OH^- \quad (4)$$

This forms a passive barrier film over the substrate that protects it from further corrosion [16] (17).

1.6.4. $Ce(NO_3)_3$ and $La(NO_3)_3$

Cerium and lanthanum ions are well-known anticorrosion inhibitors (18)[19]. They work as a cathodic inhibitors by growing a hydroxide film over the cathodic surface when being in the presence of HO^- formed by oxygen reduction reaction.

In an aqueous solution the reaction (5) occurs, giving the insoluble rare earth (RE) metal hydroxide [4].

$$RE^{3+} + 3OH^- = RE(OH)^3 \quad (5)$$

And further oxidation of the RE(III) leads to the formation of RE(IV), according with to the reaction 6.

$$4RE(HO)_3 + O_2 = 4\ REO_2 + 6H_2O \quad (6)$$

The inhibition efficiency depends on properties of the formed film, as its density is influenced by cathodic currents. Strong cathodic currents give rise to porous films.

1.6.5. BIA

BIA also called 1,3-Benzimidazole, or BZI is an organic corrosion inhibitor. Figure 9 shows the structure of BIA. The compound works by complexation with copper, as NHC's are known to form transition metal complexes and creates a passive layer on the copper surface, when this is immersed in a solution containing BIA. The exact structure of the complex is not known.

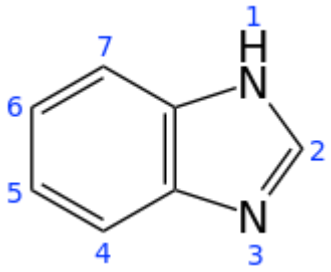

Figure 9. Structure of BIA

1.6.6. BTA

BTA also known as 1,2,3-benzotriazole or 1H-benzotriazole is the second organic inhibitors being used in this work. Figure 10 shows the tautomer structures of BTA. At room temperature the structure A is found to be the most common.

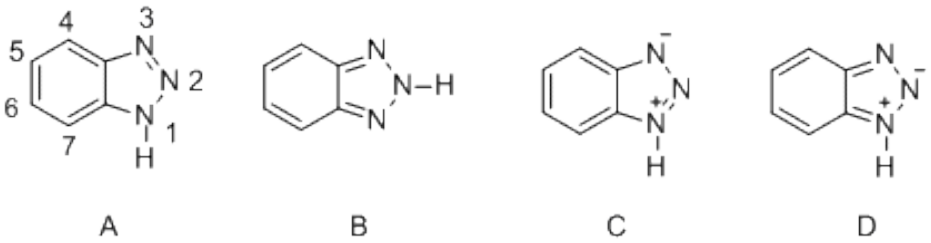

Figure 10. Various tautomer structures of BTA

This is a common inhibitor used for copper and copper alloys [20]. It forms a passive layer by complexation with the copper surface, when immersed in a BTA solution.

This passive layer is stable in aqueous and some organic solutions. The exact complexion mechanism on the surface is not known, Figure 11 shows one of the proposed structures.

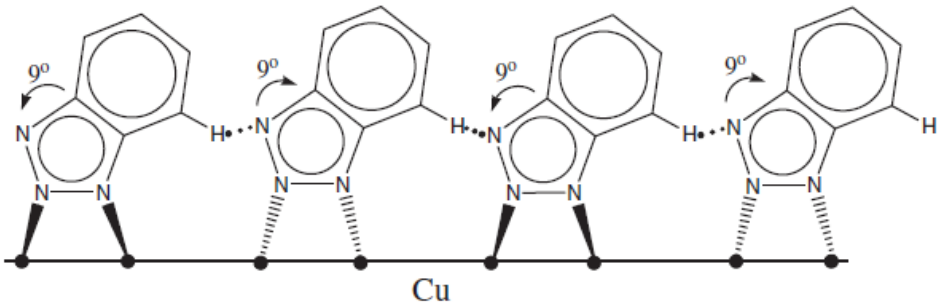

Figure 11. "Structure of the first chemisorbed layer, proposed by Fang et al" [20].

1.7. Methodologies

1.7.1. ZRA

In the Zero Resistance Ammeter (ZRA) two electrically linked samples are immersed in a solution. This setup forms a galvanic system with an anode and cathode and current flowing between them. The idea of the measurement is to register this current with sensitive ammeter.

The ZRA counters the effect of the inserted resistance by applying a voltage across the resistor from within the instrument that is exactly equal to the voltage drop across the resistor. This applied voltage is divided by the resistance and reported as the current in the circuit. As there is no burden on the measured circuit, the reported current is exactly correct [21].

1.7.2. EIS

Electrochemical Impedance spectroscopy (EIS) is a common technique to understand mechanisms and kinetics involved in electrode reaction in various environments. The technique works by applying an electrical AC perturbation, in a sinusoidal manner, to a system and measuring the systems electrical response. In usual cases the spectrometer carries out the measurement in a range of frequencies and measures these two entities along the frequency range.

One parameter measured is the phase shift between the crest of the electrical stimuli and the crest of the response, as well as the ratio of current to voltage. A representation of this shift and ratio can be seen in Figure 12.

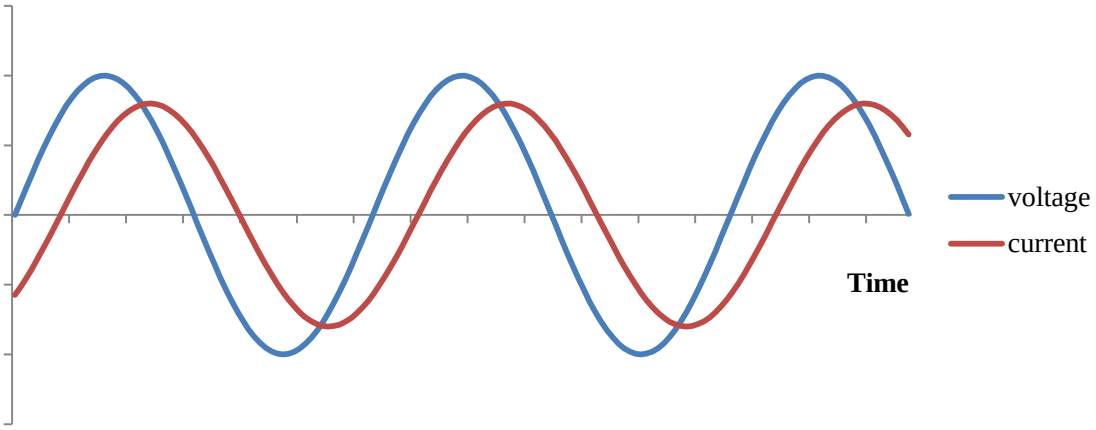

Figure 12. Representation of common current response when AC stimuli is applied.

Impedance is a complex entity containing a real and imaginary component, if these are plotted in the Argand plane we get a Nyquist diagram, like the one in Figure 13.

In potentiostatic impedance by applying Equation 1 we can calculate the norm of the complex quantity and by relating it to the phase shift one can deconstruct the real and imaginary components.

$$|Z| = \frac{V0}{I0} \cdot \frac{sin\omega t}{sin(\omega t + \varphi)} \qquad \text{Equation 1}$$

Where V_0 is the amplitude of the stimuli, I_0 is the amplitude of the current response, t is time, ω is the angular frequency and φ is the phase shift (22).

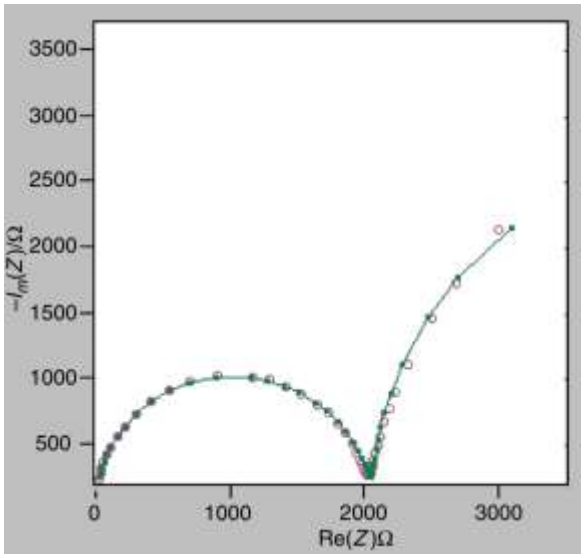

Figure 13. Typical Nyquist diagram plot (22)

A different type of representation can be made by plotting |Z| or φ versus ω or frequency on logarithmic scales, as showed in Figure 14. This helps in the visualization of certain behaviors, which are orders of magnitude smaller and are harder to distinguish in the Nyquist plot.

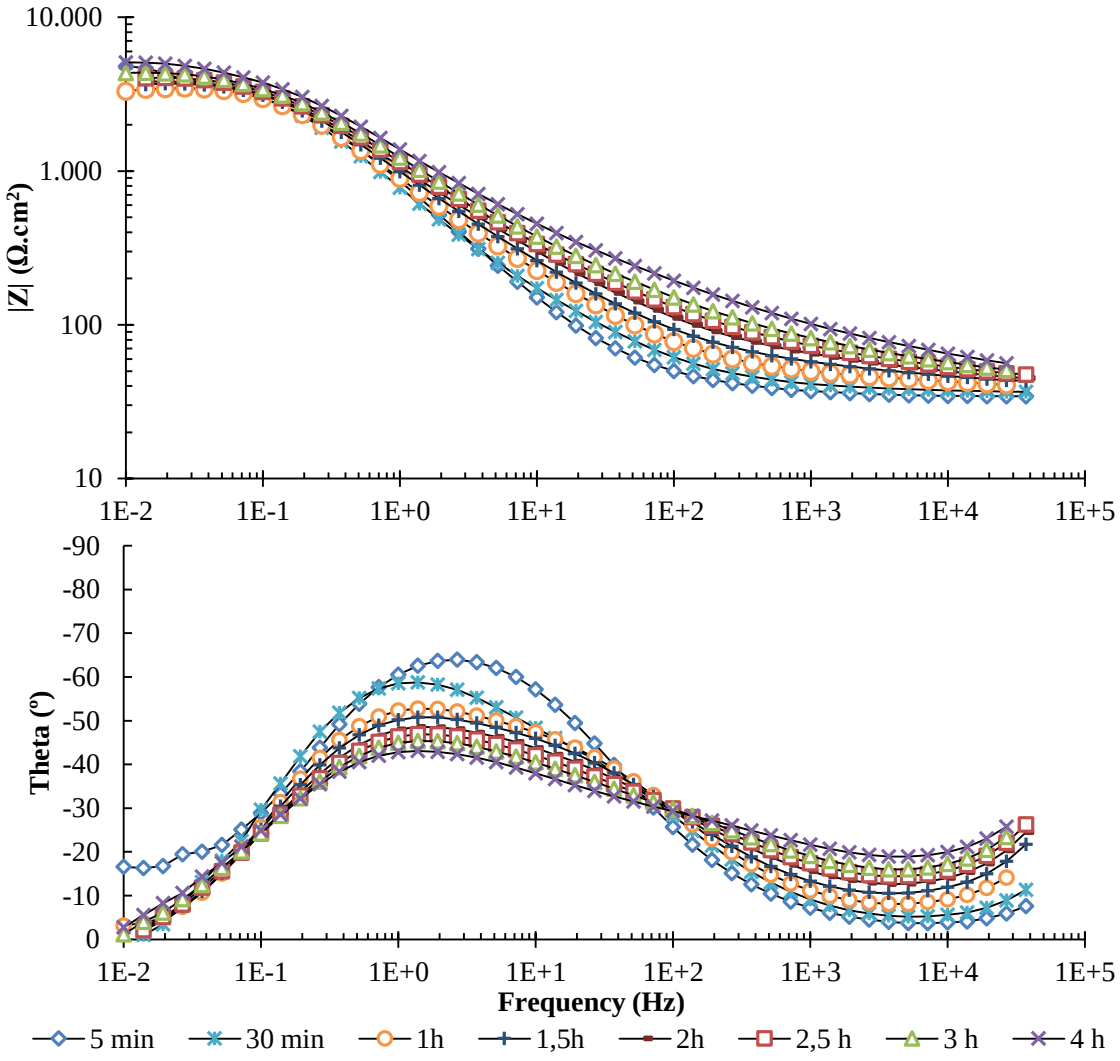

Figure 14. Bode plot

1.7.3. SVET

Scanning Vibrating Electrode Technique (SVET) is a relatively new technique in corrosion, introduced from the biology sciences in the 80's by Hugh Isaacs (23).

The experimental set up is composed by a vibrating electrode that rasters the sample area at a fixed distance from the sample while immersed in the test medium, as showed in Figure 15 b). In Figure 15 a) the vibration of the tip can be seen. The tip vibrates at frequencies of 100Hz to 1000Hz along the X and Z axis (23).

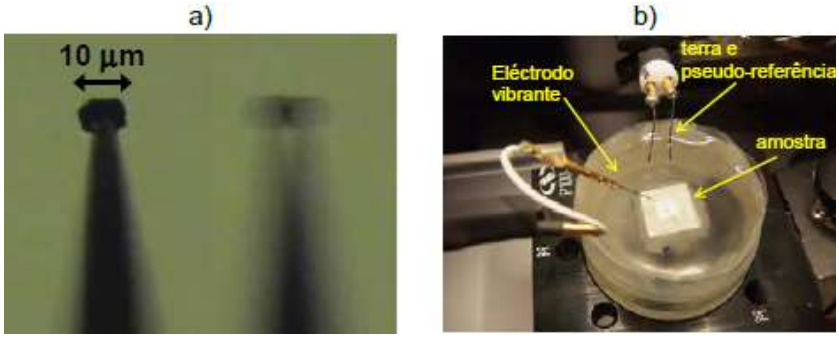

Figure 15. a) vibrating electrode b) experimental set up (23)

This technique works by measuring the potential difference created by ionic fluxes going towards and away from the electrochemically active sites. As the tip vibrates it measures the local potential difference between the extreme positions of vibration in regards to the reference electrode. By proper calibration the voltage can be converted into current and a map-like display can be presented as showed in Figure 16.

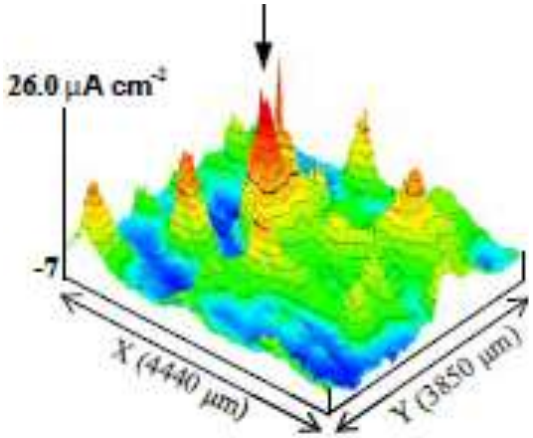

Figure 16. SVET map of current intensities at a given distance from the sample (23)

Common limitations of the technique are the fact that it gives no information about the ionic species, only the fluxes. Another problem is when the area rastered is not well chosen and the partial current activity takes place under the measurement level, as represented in Figure 17 a), or only a small part of the currents is actually inside the measurement area, as represented in Figure 17 b).

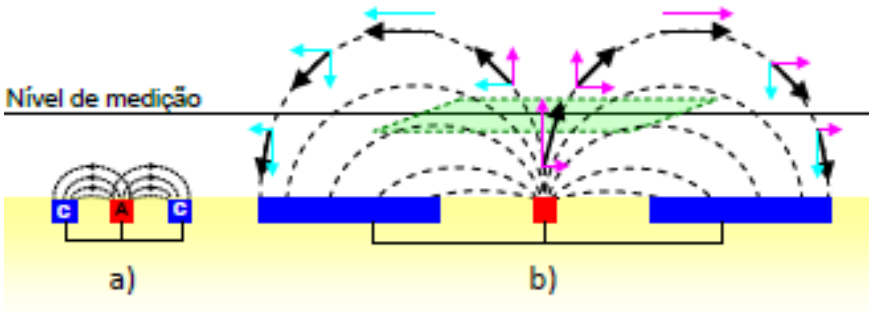

Figure 17. Representation of some SVET limitations (23)

The main advantages are that it is not an invasive technique, so the reactions on the surface are not disturbed by the probing and that it does a localized approach, allowing the distinction of the anodic and cathodic active sites in the sample.

2. Experimental

2.1. Galvanic corrosion measurements on Zn-Fe

For initial testing of the corrosion measurements an iron coupled with zinc electrode (Fe-Zn) was chosen. Zinc and iron rods with 1cm diameter were cut and embedded in commercially available clear epoxy resin. The mounts were shaped and glued together as can be seen in Figure 18. The metals were isolated with beeswax or Apiezon wax to prevent crevice corrosion in the epoxy resin and metal interface.

Figure 18. Working electrode formed by zinc in red and iron in black electrically linked.

The surface of the electrodes were routinely polished by hand before every experiment until they seemed pristine to the naked eye.

In Figure 19 a) the schematic image of the classical three electrode electrochemistry setup is shown, in which the working electrode is composed of only one material. In Figure 19 b) the novel approach is shown where the working electrode is composed of two separate electrically linked materials.

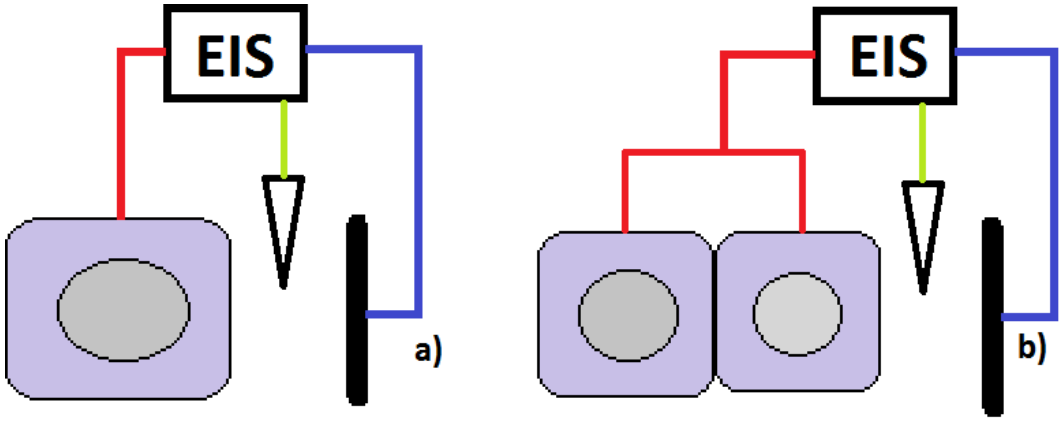

Figure 19. a) Classic electrochemistry setup, b) approach tried in this work for galvanic systems.

The samples were then immersed in the different test-mediums in 100ml cups. A platinum wire was used as a counter electrode and a Radiometer analytical SCE was used as reference, as can be seen in Figure 20.

Figure 20. Mounted electrochemical cell.

The EIS was made by sampling 50 logarithmically distributed points over a frequency range of 100 kHz to 10 mHz and with an perturbation amplitude of 10 mV (RMS). The EIS data was analyzed using Zview (Scribner Associates) software.

The electrochemical measurements were done using Autolab PGSTAT302N hardware and FRA 4.9.007 software. Whole electrochemical setup was shielded in Faraday cage (Figure 21).

Figure 21. EIS measurement apparatus.

Table 1 and Table 2, show us a list of all examined inhibitor and substrate systems as well as all the mediums tested.

In Table 2 the compositions and concentrations of tested inhibitor mixtures are displayed. The inhibitor concentration of each member of the mixture is half of the standalone systems. This was done so that the total concentration of inhibitors in the immersion medium is the same as in the case of the single inhibitors, so that the data would be more comparable.

Table 1. Single inhibitor systems

	Fe-Zn	Fe	Zn
NaCl [50mM]	3 X	X	X
NaCl [50mM] + $NaWO_4$ [5mM]	X		
NaCl [50mM] + $NaVO_3$ [5mM]	X		
NaCl [50mM] + $K_2Cr_2O_7$ [5mM]	X		
NaCl [50mM] + $NaMO_4$ [5mM]	X		
NaCl [50mM] + Na_2HPO_4 [5mM]	X		
NaCl [50mM] + NaH_2PO_4 [5mM]	X		
NaCl [50mM] + $Ce(NO_3)_3$ [5mM]	X		
NaCl [50mM] + $La(NO_3)_3$ [5mM]	X		
NaCl [50mM] +BIA [5mM]	X		
NaCl [50mM] + BTA [5mM]	X		

Table 2. Mixture of inhibitors

	Fe-Zn	Fe	Zn
NaCl [50mM] + BTA [2,5mM] + $Ce(NO_3)_3$ [2,5mM]	X	X	X
NaCl [50mM] + BIA [2,5mM] + $Ce(NO_3)_3$ [2,5mM]	X		

2.2. Galvanic corrosion in AA2024 and CFRP

For testing the AA2024-CFRP galvanic system the test samples were mounted in a cuboid sample holders showed in Figure 22. The volume of the cell is 0.357 liters and the distance between electrodes is of 64 mm with an electrode (single) area of 1050 mm². The samples were fixed to the sample holder using ELASTOSIL ® RT 622 A/B. For the measurements a SI Analytics SCE and a platinum sheet were used as reference and counter electrode respectively.

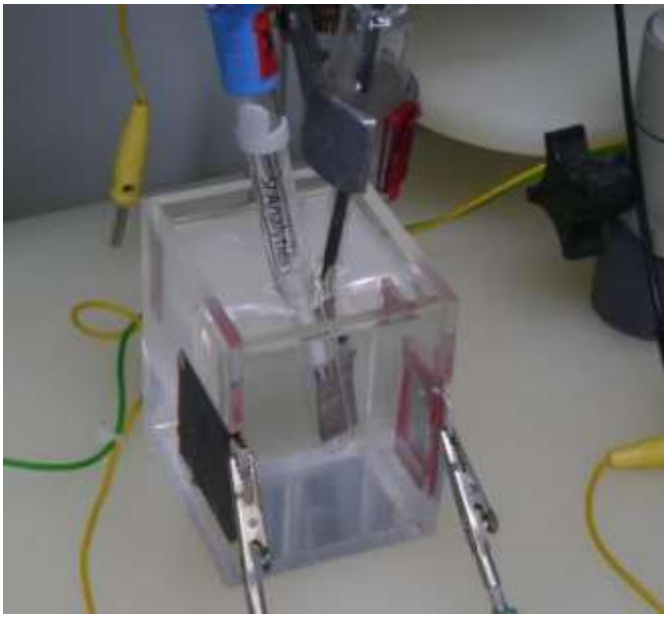

Figure 22. Experimental setup used in Airbus for electrochemical measurements.

The solutions were prepared using commercially available powdered substances.

The data on the reagents used can be seen in Table 3

Table 3. Powder suppliers and purity, for all the systems prepared at Airbus.

Powder	Supplier	Purity
NaCl	Fluka	>99.5%
Na_2WO_4	MERCK	>99%
$NaVO_3$	MERCK	>98,5%
BIA	MERCK	>99%
BTA	BAYER	
$Ce(NO_3)_3$	Sigma-Aldrich	>99%

The CFRP samples were cut from a prepreg block with dimensions ≈ 40x50x3mm and grinded manually. The prepreg block was a quasi-isotropic laminate with different fiber orientations (Figure 23). The samples were mounted so that the electrode area was the cross section perpendicular to the laminates. Also the edges perpendicular to the laminates were covered with silver-paint in order to ensure inter-laminate conductivity.

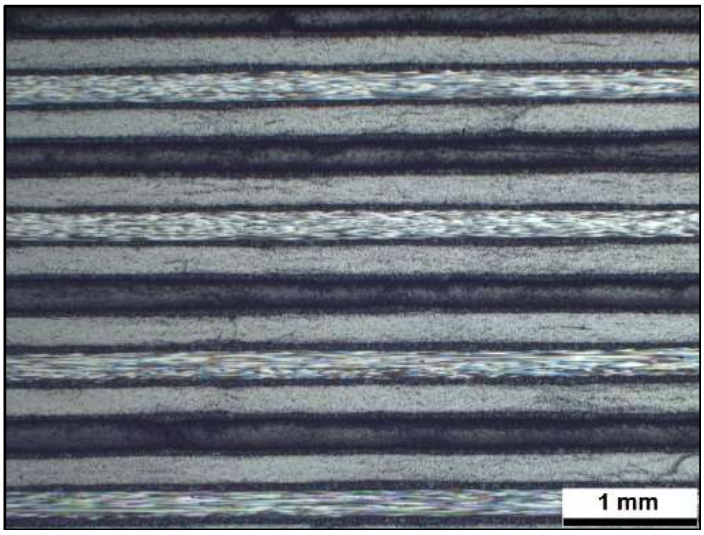

Figure 23. CFRP sample

The AA2024 samples were cut from bigger sheets that have been manually grinded and mounted in the cells using the Elastosil. And finally cured in the oven between 50°C - 60°C.

In Table 4 the studied systems are presented. Usually the samples were immersed for up to 48h. In the case of coupled systems the ZRA measurements were temporarily stopped at 1h, 5h, 10h, 24h, and 48h for impedance measurements and continued later. In case of single electrode systems only impedance measurements were made.

The artificially polarized systems were galvanostatically polarized with the currents observed previously during the ZRA measurements on the natural couple. The cell potential was measured during this galvanostatic polarization. Then polarization was stopped and potentiostatic impedance measurements were done using the previously measured potential. When finished polarization was resumed.

Table 4. Coupled and single electrode systems studied. Artificial polarization values for the AA2024 samples and for the CFRP.

	AA2024 - CFRP	AA2024	CFRP	AA2024 pol. mA/cm^2
NaCl [50mM]	X	X	X	0,13
NaCl [50mM] + $NaWO_4$ [5mM]	X	X	X	0,11
NaCl [50mM] + $NaVO_3$ [5mM]	X	X		0,07
NaCl [50mM] + BTA [5mM]	X	X		0,08
NaCl [50mM] + BIA [5mM]	X	X		0,12
NaCl [50mM] + BTA [2,5mM]+ $Ce(NO_3)_3$ [2,5mM]	X	X		0,04

The electrochemical measurements were made using Autolab PGSTAT302N hardware and Nova 1.10 software in a Faraday cage as can be seen in Figure 24.

Figure 24. Autolab and Faraday cage for electrochemical measurments.

The ZRA was made using sampling time of 2 seconds. The calculation of the mean potential and mean current were made using only the final sampling period of 24h.

The EIS was made by sampling 70 points logarithmically distributed over a frequency range of 100 kHz to 10 mHz and with an AC perturbation amplitude of 10 mV. The EIS data was analyzed using ZView (Scribner Associates) software.

Conductivity and pH of the solutions were measured. The pH measurements were done using a WTW pH1970i and conductivity was measured with a WTW microprocessor conductivity meter.

After at least 48h of immersion time the pictures of aluminium samples were taken manually using a commercial camera.

2.3. Data treatment

In the case of galvanic systems the EIS data was normalized to anode surface area and the cathode as a not actively dissolving/corroding but just an influencing part of the system was discarded from active area calculations

Inhibition efficiency for ZRA data was calculated using Equation 2.

$$\text{Inhibitor efficiency} = 100 \times \frac{I_{ref}-I_{inh}}{I_{ref}} \qquad \text{Equation 2}$$

In which I_{ref} is the current in NaCl reference corrosive media and I_{inh} is the current in system where we are trying to determine the efficiency from.

When using Rpol or |Z| to determine the inhibitor efficiency these were converted to corrosion rates, which is the reciprocal of these showed in Equation 3.

$$\text{Inhibitor efficiency} = 100 \times \frac{\frac{1}{\text{Rpol}_{ref}} - \frac{1}{\text{Rpol}_{inh}}}{\frac{1}{\text{Rpol}_{ref}}} \qquad \text{Equation 3}$$

For EIS modelling two different types of equivalent circuits were used, one for systems with one time constant and other for systems with more (Figure 25). In which Rsol is the resistance of the electrolyte solution, CPE dl is the constant phase element that represents the capacitance response of the double layer, Rpol is the polarization resistance, CPE 1 represents the capacitance response of the adlayer and R1 is the adlayer resistance.

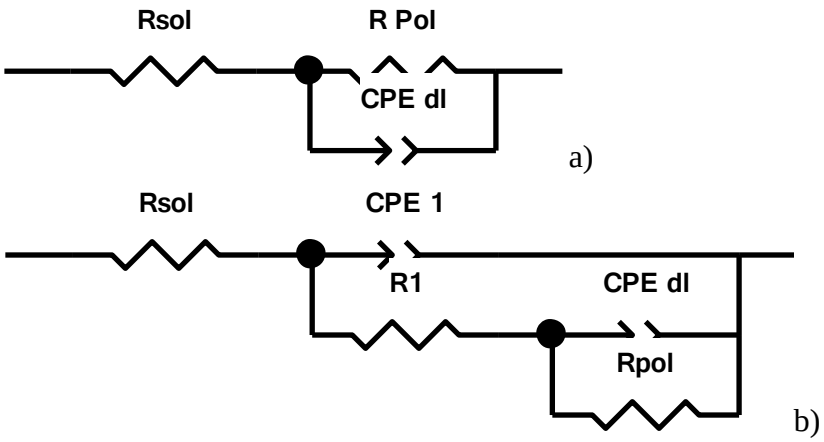

Figure 25. Equivalent circuits used in the fittings a) for one time constant and b) for two.

To calculate the synergistic parameter (S) Equation 4 by Aramaki and Hackerman[24] was used.

$$S = \frac{1 - IE_{1+2}}{1 - IE_{12}} \qquad \text{Equation 4}$$

Where $IE_{1+2} = (IE_1+IE_2)-(IE_1 x IE_2)$. And the parameters IE_1, IE_2 and IE_{12} are the inhibition efficiencies of inhibitors 1, 2 and mixture of 1 and 2. If S value is higher than 1 than there is a synergistic behavior [24].

3. Results and Discussion

3.1. Galvanic corrosion on Iron and Zinc

Bare Iron and Zinc samples were measured in steady state conditions in a sodium chloride (50mM) aqueous solution and in the presence of the inhibitor mixture BTA + $Ce(NO_3)_3$. The results were then compared with the galvanically linked electrodes, which were tested in a wider range of inhibitors.

Table 5 shows the solution conductivities measured in the beginning of the EIS measurements.

Table 5. Solution conductivity after 5 min of immersion calculated using the EIS data fittings at Zn-Fe galvanic system.

	Conductivity (S/cm)
NaCl [50mM]	0,040
NaCl [50mM] + Na_2WO_4 [5mM]	0,059
NaCl [50mM] + $NaVO_3$ [5mM]	0,041
NaCl [50mM] + $K_2Cr_2O_7$ [5mM]	0,042
NaCl [50mM] + Na_2MO_4 [5mM]	0,036
NaCl [50mM] + Na_2HPO_4 [5mM]	0,038
NaCl [50mM] + NaH_2PO_4 [5mM]	0,039
NaCl [50mM] + $Ce(NO_3)_3$ [5mM]	0,056
NaCl [50mM] + $La(NO_3)_3$ [5mM]	0,065
NaCl [50mM] + BIA [5mM]	0,045
NaCl [50mM] + BTA [5mM]	0,052
NaCl [50mM] + BTA [2,5mM]+ $Ce(NO_3)_3$ [2,5mM]	0,079

3.1.1. EIS measurements on single electrodes

Figure 26 shows the bode plots of the single iron electrode immersed in the reference solution (represented with circles in the graph) and in the presence of BTA + $Ce(NO_3)_3$ mixture, represented with triangles.

As it can be seen the black lines that represent 30min of immersion almost overlay each other perfectly, but as time goes by the reference shows signs of corrosion processes taking place as the total impedance goes down and corrosion advances.

The inhibitor on the other hand shows signs of inhibition taking place as the impedance goes up as time goes by, this could be attributed to a thin adsorption adlayer of inhibitor being formed on the surface.

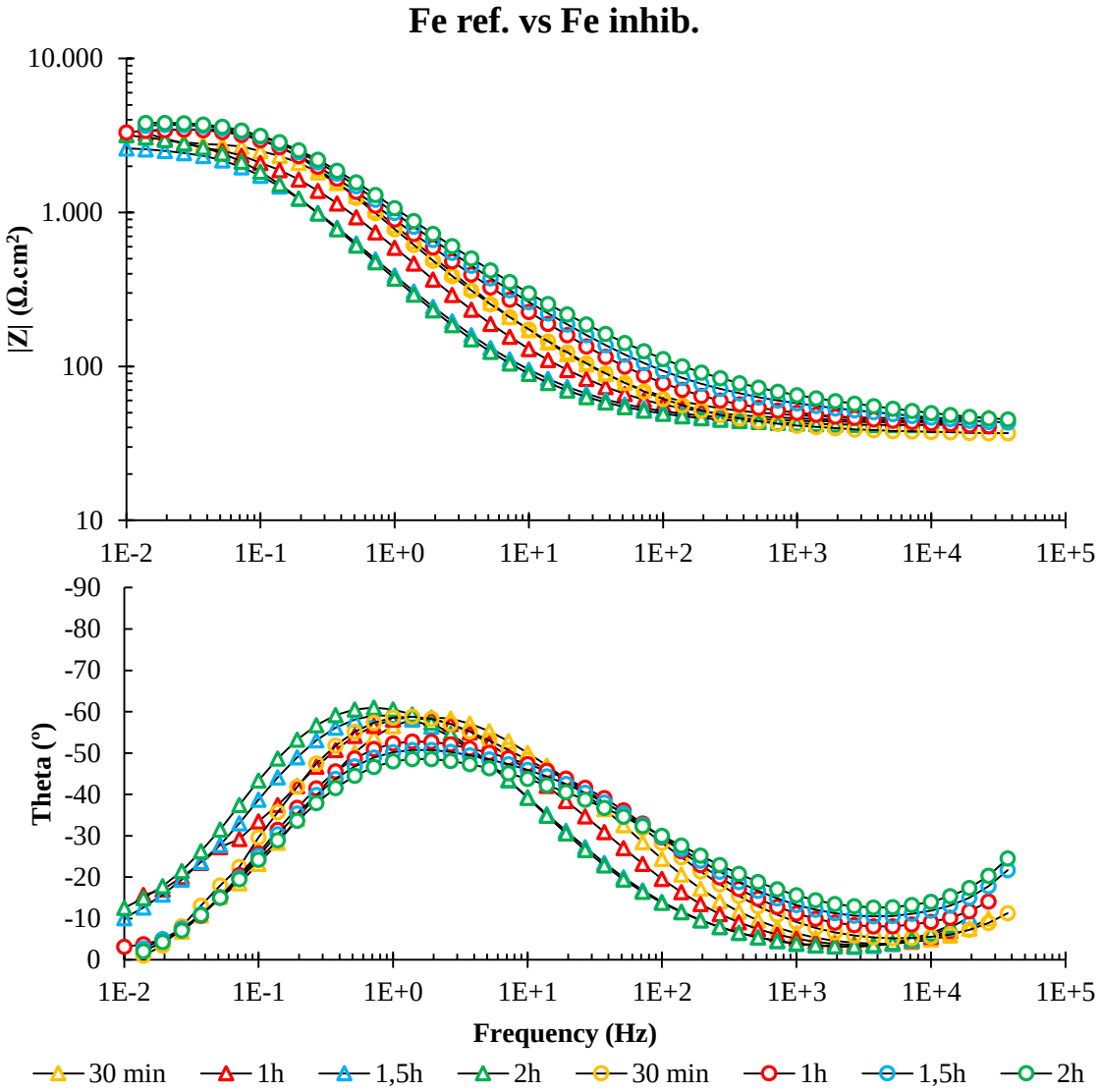

Figure 26. Bode plots for the iron single electrode in ref. solution (triangles) and the inhibitor mixture (circles).

Figure 27 shows a drastic difference when comparing the iron systems with the zinc. The two biggest differences are the initial difference between the impedances about 2 orders of magnitude, when comparing the inhibitor containing system and the reference solution. And the reference system shows a faster impedance drop over time. The bigger drop in the case of reference system is understandable as the zinc is a more active material and corrodes faster.

In the phase shift bode plot a time constant appears in the very low frequencies and grows with time. This has been attributed to either corrosion products of zinc forming on the surface, or it could be due to oxygen deficiency in the electrolyte.

The initial difference in impedance shows that the inhibitors work better on a zinc substrate. It is in accordance with previous works which point to that BTA forms complexes with zinc ions [25][26][27].

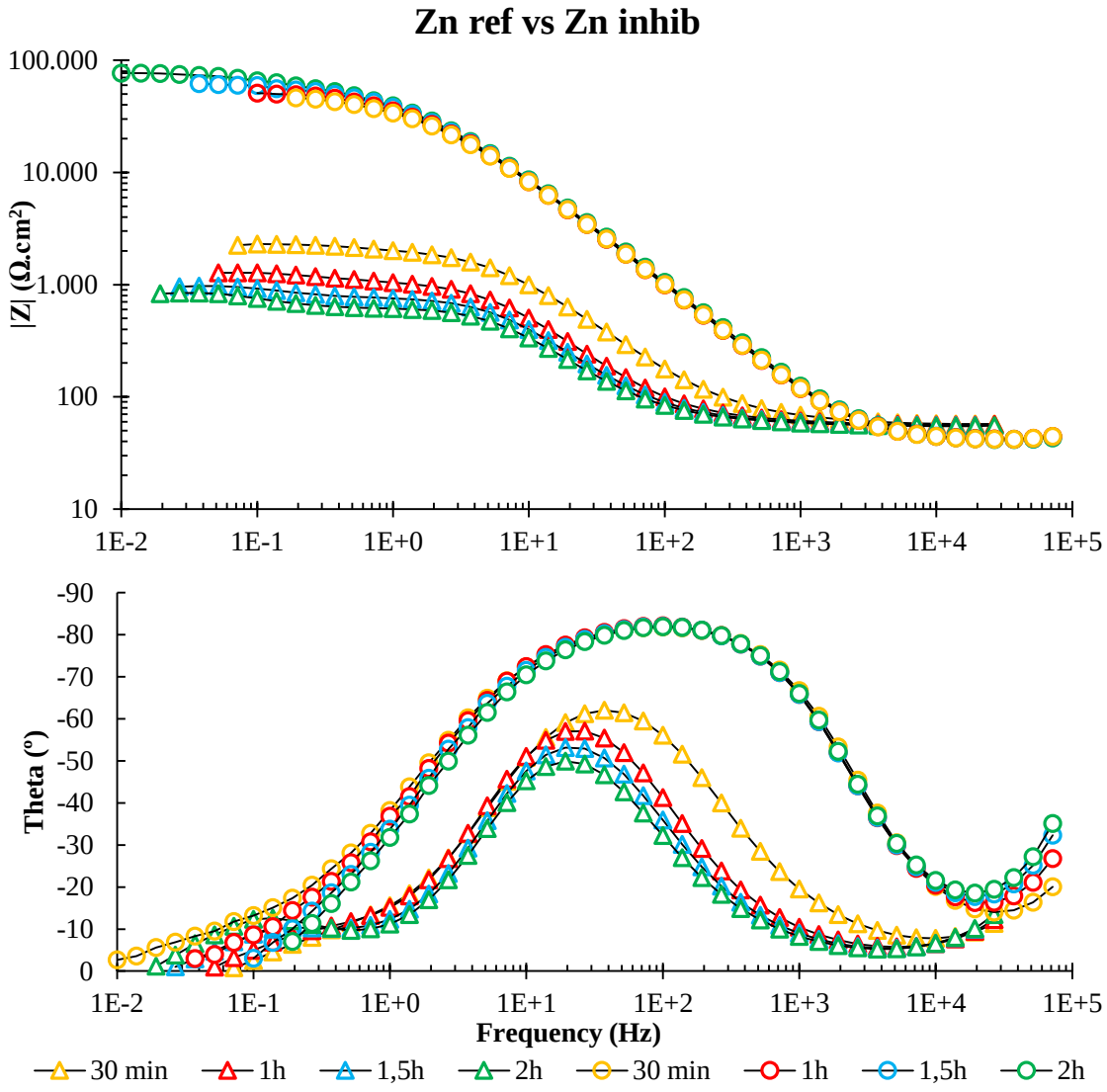

Figure 27. Bode plots for the zinc single electrode in ref. solution (triangles) and the inhibitor mixture (circles).

By plotting the total impedance values measured at 0,1Hz of the various samples impedance evolution over time can be seen. This is represented in Figure 28, the same treatment can be made with the Rpol value after fitting the EIS curves (Figure 29).

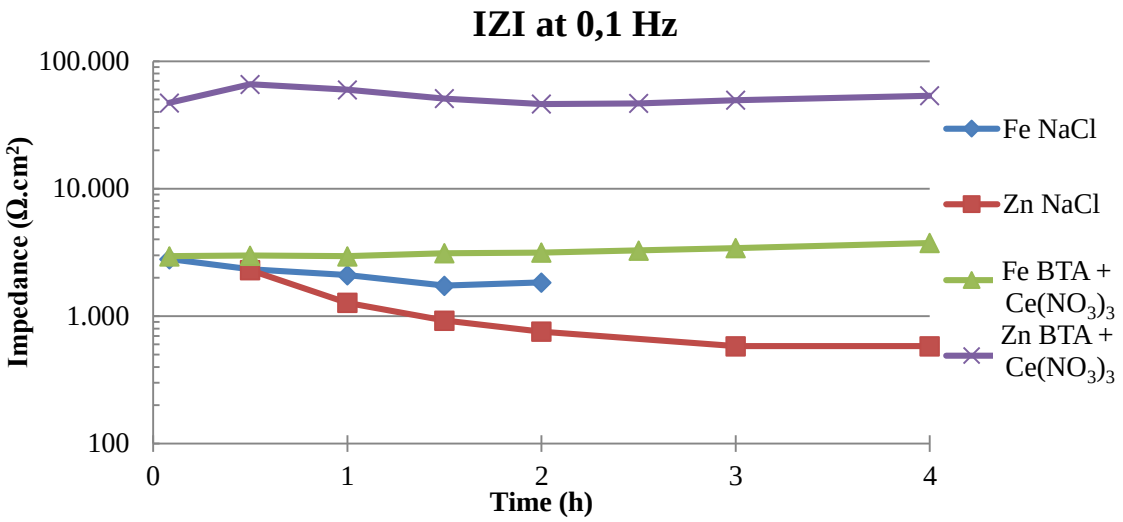

Figure 28. Impedance evolution over time for the single electrodes on reference solution and inhibitors mixture.

Figure 28 shows that although the inhibition was observed in both cases the zinc substrate was better inhibited by the mixture of inhibitors. In the case of iron electrode although there is some improvement it is not that pronounced.

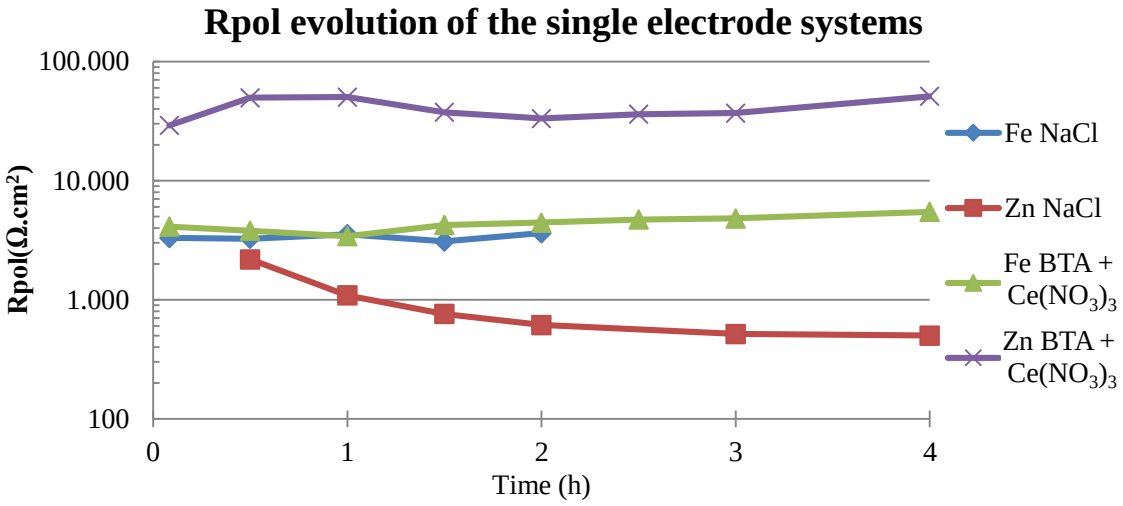

Figure 29. Polarization resistance evolution over time for the single electrodes on reference solution and inhibitors mixture.

The same conclusions can be taken from Figure 29, but the effect on the iron electrode is even smaller.

By using Equation 3 the inhibition efficiency was calculated and presented in Figure 30. Here we can see that the inhibition of the zinc substrate corrosion was in fact particularly high.

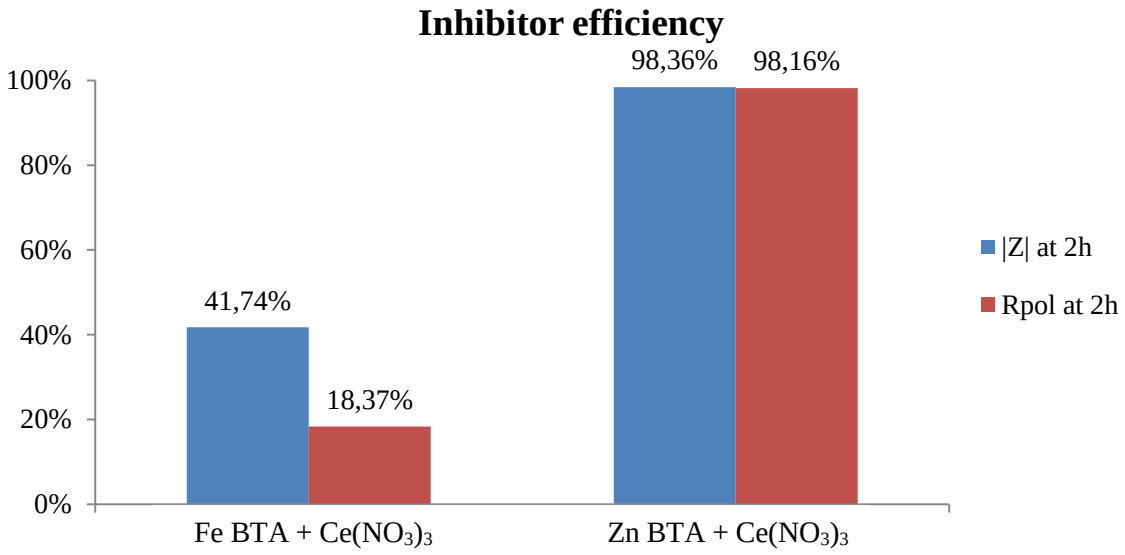

Figure 30. Inhibitor efficiency for the single electrodes calculated using Rpol and |Z| values for the corrosion rate at 2h of immersion time.

3.1.2. EIS measurements GC

After single electrode measurements were done the Fe and Zn electrodes were electrically linked and EIS measurements were done.

Figure 31 shows the bode plots of the reference system (Fe-Zn electrode in a 50mM of Cl^-). This was done 3 times for the sake of consistency. And as it can be seen the reference system is reproducible.

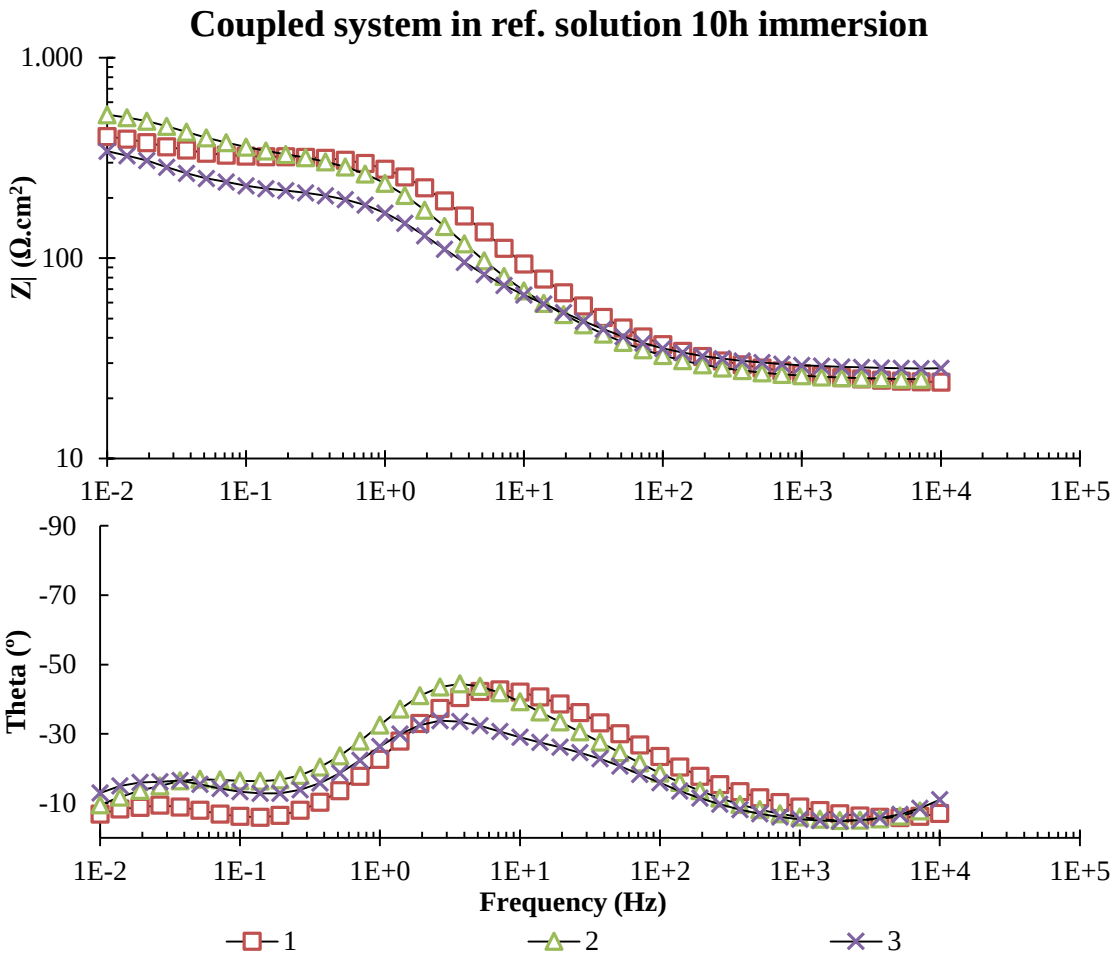

Figure 31. Bode plots of the Fe-Zn galvanic couple in reference solution, at the 10h of immersion measurement, in 3 different samples.

Figure 32 shows the EIS data for all the inhibitor systems after 12 hours of immersion. As it can be seen these are very different from each other.

The mixture of inhibitors (BTA + $Ce(NO_3)_3$) shows a clear superiority to all other inhibitors, even though when these same inhibitors used in the mixture are not that efficient separately. For instance $Ce(NO_3)_3$ even had a detrimental effect. So there is clearly some apparent synergistic effect presented that improves the inhibition especially when the galvanic corrosion occurs.

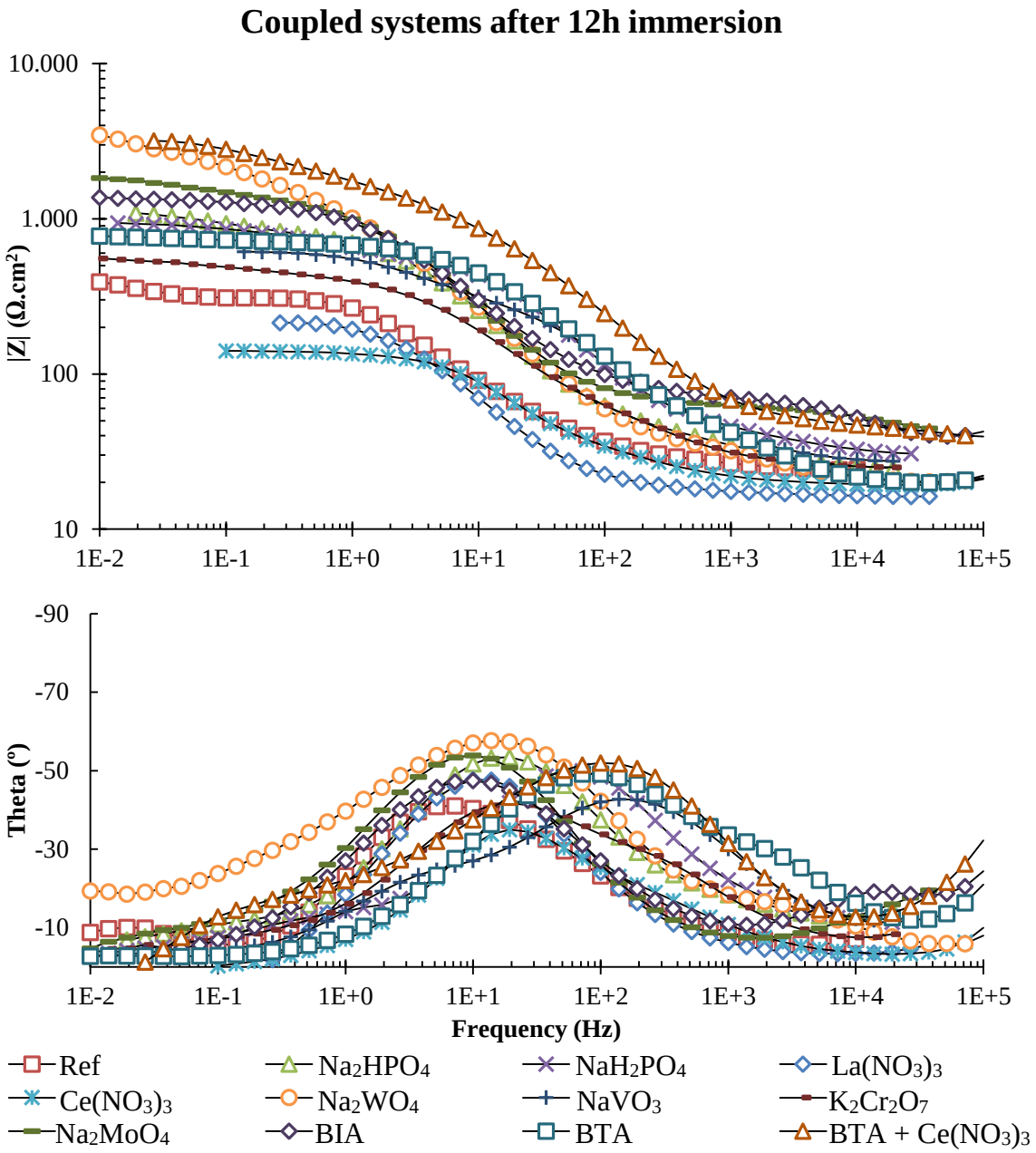

Figure 32. Bode plots of the Fe-Zn galvanic couple in all tested inhibitor systems, after 12h of immersion measurement.

In Figure 33 the EIS response over 90h can be seen. In the graph the lighter colors represent the longer immersion times and a clear evolution can be seen as time goes by.

In comparison with the reference system the clear improvement over time has demonstrated as the impedance is still more than one order of magnitude higher in case of selected inhibitor systems.

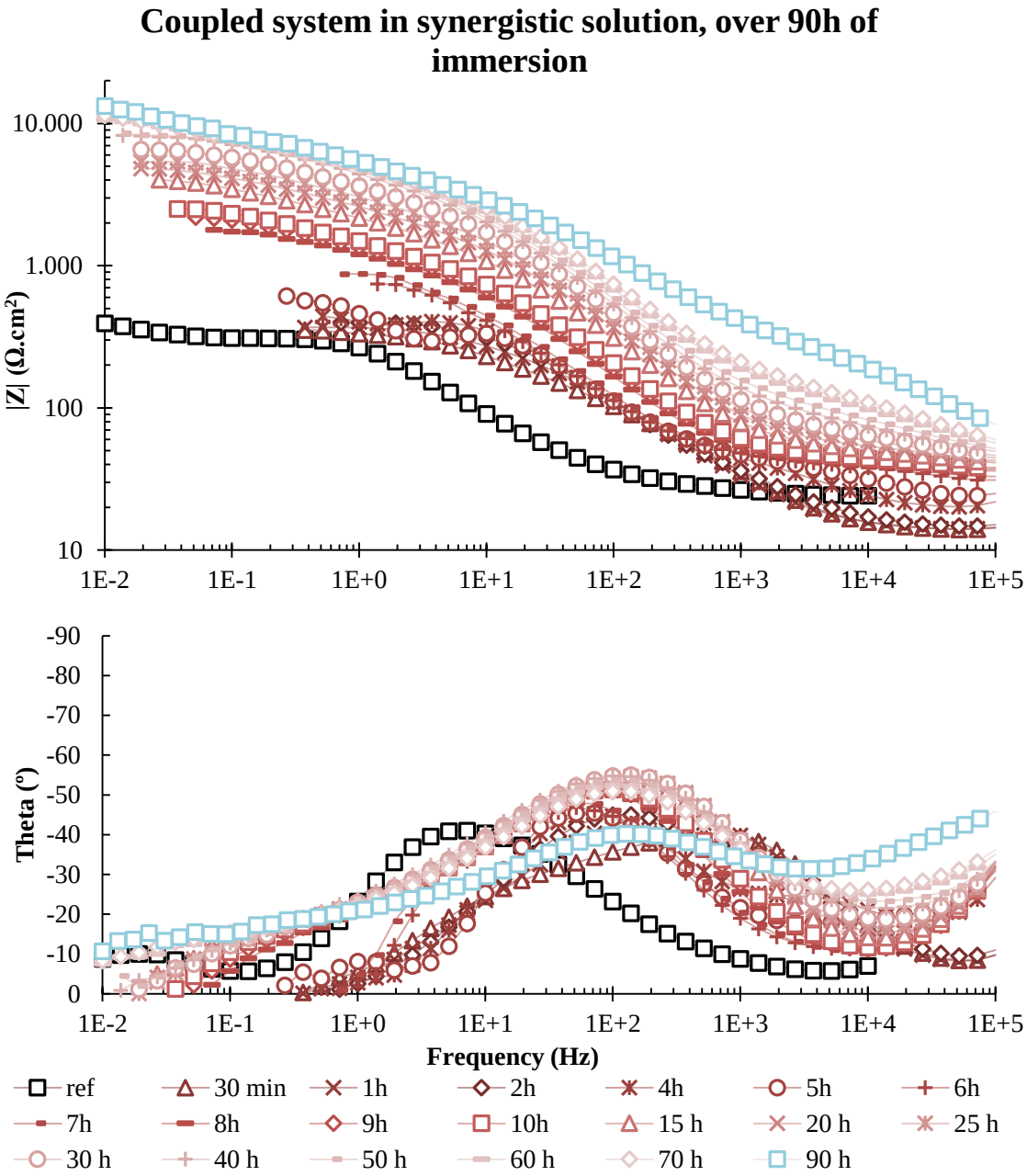

Figure 33. Bode plots of the Fe-Zn galvanic couple of the impedance response of the synergetic mixture over 90h in comparison with the 12h immersion of the reference solution.

In Table 6 the open circuit potential values of the inhibitor containing systems are shown. The data shown in red are the last values measured in systems that did not stabilize over the 12 hours of immersion time.

By comparing the values of the single electrodes with the pairs, it appears that the potential of the pair is similar to the potential of the single zinc electrode.

Table 6. Average open circuit potential values measured in the beginning of each EIS measurement.

	Potential (mV)		
	Fe-Zn	Fe	Zn
NaCl [50mM]	-0.988	-0,628	-0,986
NaCl [50mM] + Na_2WO_4 [5mM]	-0,998		
NaCl [50mM] + $NaVO_3$ [5mM]	-1,038		
NaCl [50mM] + $K_2Cr_2O_7$ [5mM]	-0,847		
NaCl [50mM] + $NaMO_4$ [5mM]	-0,943		
NaCl [50mM] + Na_2HPO_4 [5mM]	-1,019		
NaCl [50mM] + NaH_2PO_4 [5mM]	-1,043		
NaCl [50mM] + $Ce(NO_3)_3$ [5mM]	-0,829		
NaCl [50mM] + $La(NO_3)_3$ [5mM]	-0,802		
NaCl [50mM] + BIA [5mM]	-0,986		
NaCl [50mM] + BTA [5mM]	-0,891		
NaCl [50mM] + BTA [2,5mM]+ $Ce(NO_3)_3$ [2,5mM]	-0,815	-0,462	-0,815

By plotting the low frequency impedance values measured at 0,1Hz of the various systems one can see the impedance evolution over time, this is showed in Figure 34.

Special notice for the inhibitor mixture system, that starts with a lower impedance than the NaCl reference system and evolves rapidly throw-out during the immersion time. Surpassing by far the sum of the BTA and $Ce(NO_3)_3$.

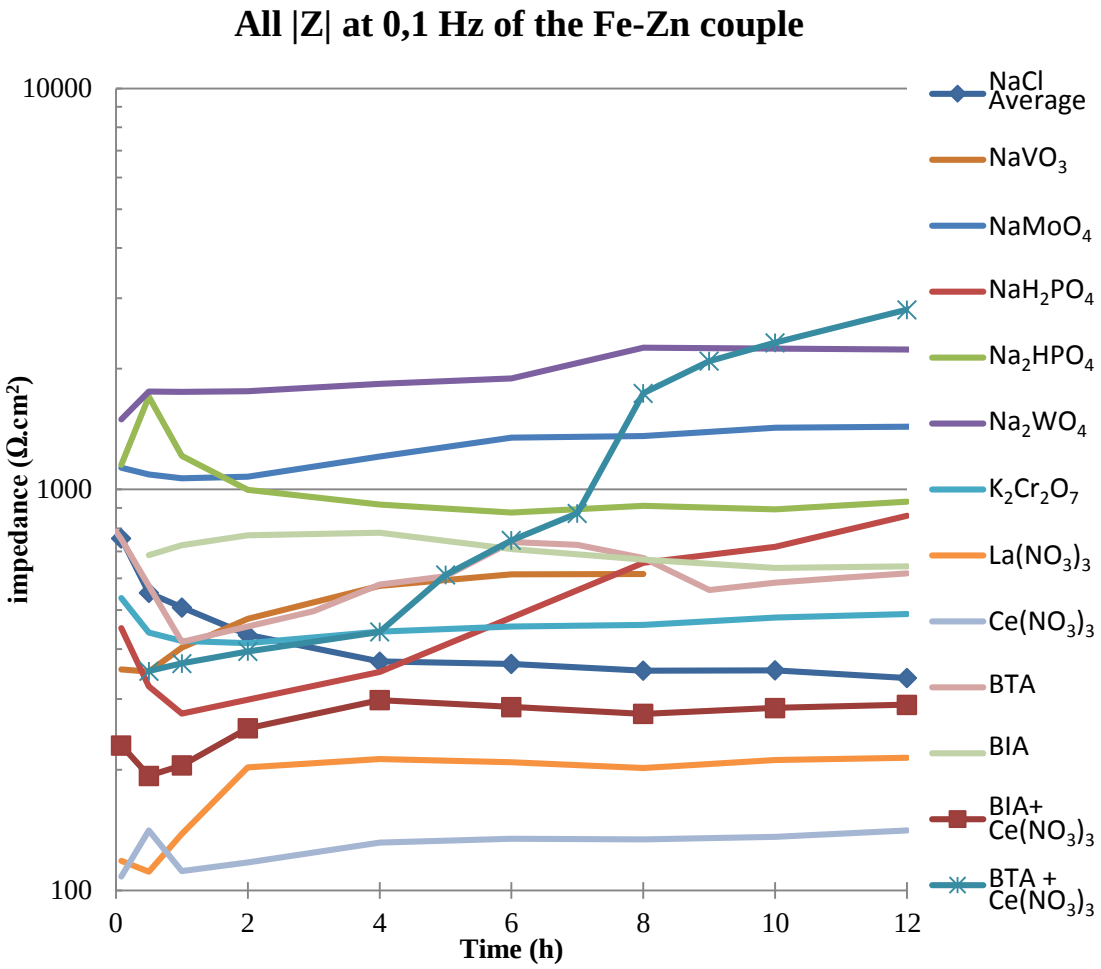

Figure 34. Impedance evolution over time of the |Z| measured at 0,1Hz for all inhibitors up to 12h of immersion for the galvanic couple.

Figure 35 shows us the impedance evolution for the Zn+Fe galvanic substrate immersed in inorganic inhibitor systems.

Remarkable is that the tungstate and molybdate systems show a clear superiority over the other systems. It can be seen that the rear earth metal nitrate solutions clearly accelerate the corrosion rate in relation to the reference system.

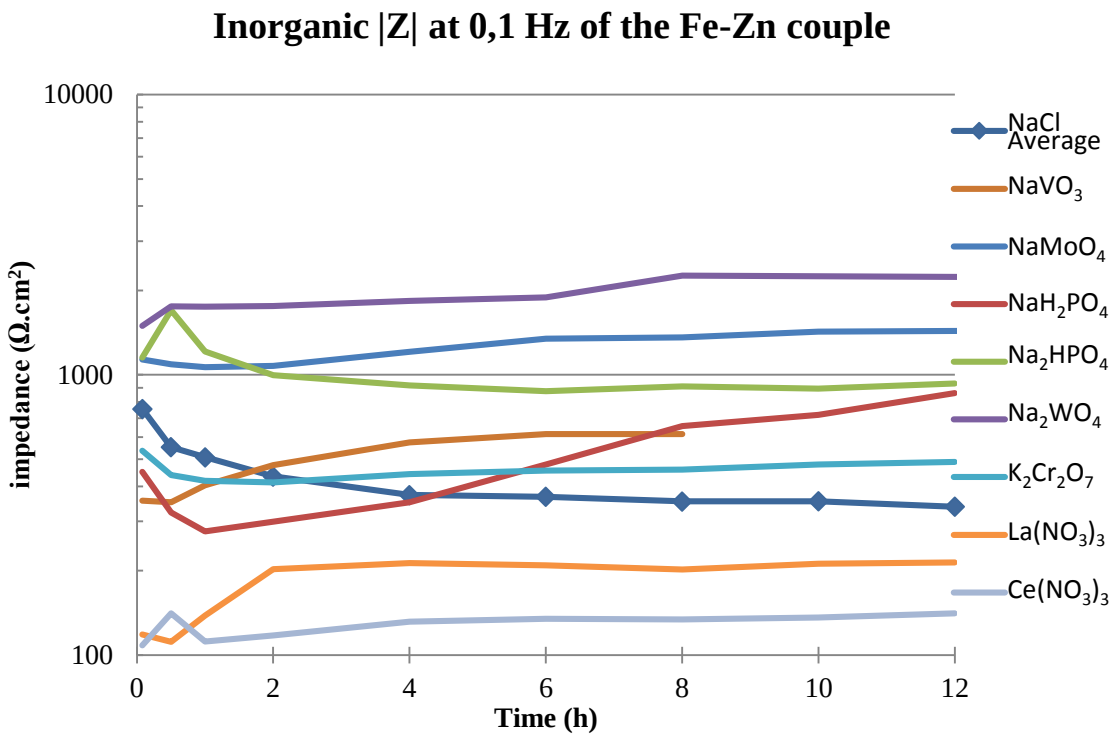

Figure 35. Impedance evolution over time of the |Z| measured at 0,1Hz for inorganic inhibitors up to 12h of immersion for the galvanic couple.

Figure 36 shows us the impedance evolution for the Zn + Fe substrate immersed in organic inhibitor systems.

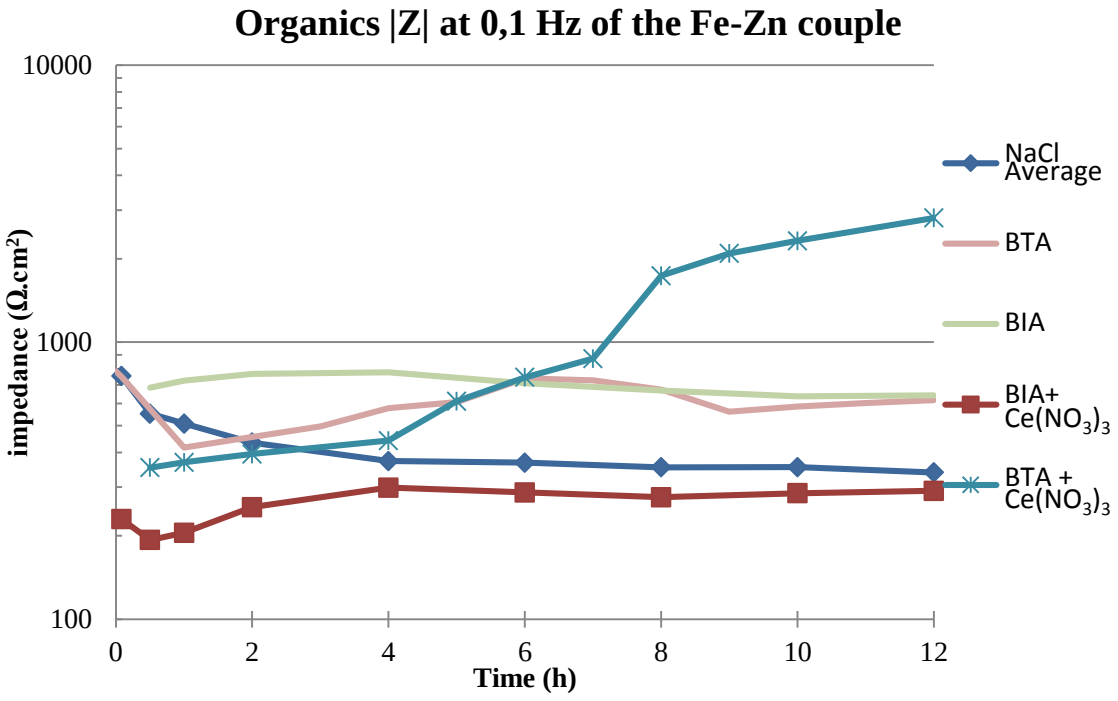

Figure 36. Impedance evolution over time of the |Z| measured at 0,1Hz for organic and mixture of inhibitors up to 12h of immersion for the galvanic couple.

Since one of the objectives of this work is the better understanding of the inhibitor mixture systems a higher time of immersion was analyze. The selected impedance evolution plots for longer testing time are presented in Figure 37.

The impedance of BTA + $Ce(NO_3)_3$ inhibitor mixture system shows promising results as it improves various orders of magnitude over the time of immersion. It shows that this mixture of inhibitors needs also some time to achieve its superior protection properties for galvanic corrosion attack.

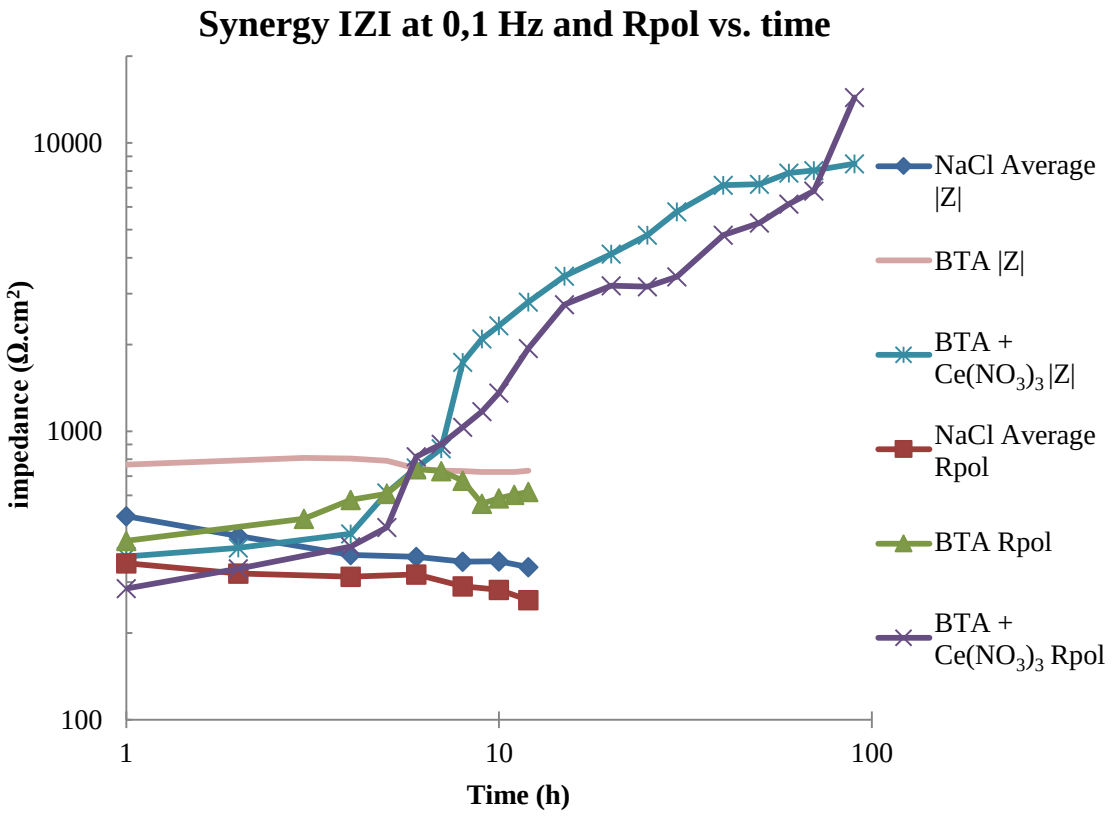

Figure 37. Impedance and Rpol evolution over time, for inhibitor mixture in comparison with the reference solution for the Zn+Fe galvanic couple.

By plotting the time evolution of the fitted Rpol parameter for all the inhibitor containing systems (Figure 38) we can see that it follows the same trend as the low frequency impedance values as it was expected. Here also some single inhibitors such as tungstate, molybdate, BIA and the BTA + $Ce(NO_3)_3$ mixture are showing somewhat promising results.

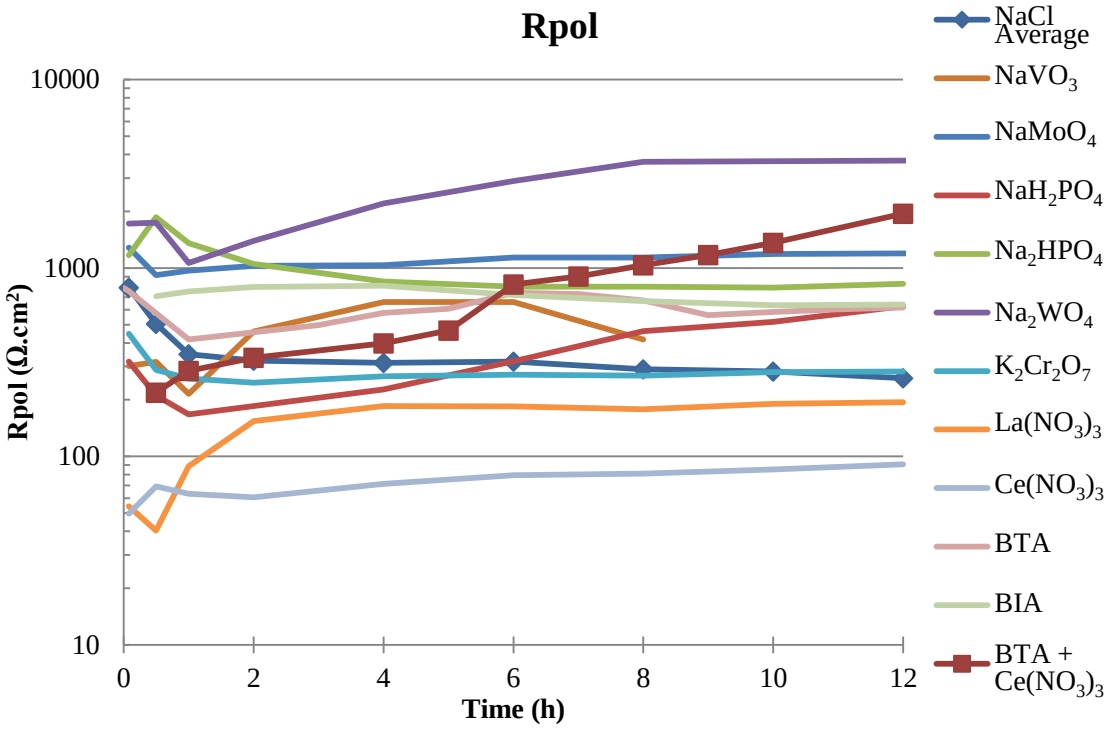

Figure 38. Rpol evolution over time of the values fitted from the EIS data for all inhibitors up to 12h of immersion for the Zn+Fe galvanic couple.

By using Equation 3 with the Rpol and |Z| values, the inhibition efficiency can be calculated.

Figure 39 shows the inhibition efficiency after 12 hours of immersion. It is easy to see the improvement of the inhibitor mixture over the single inhibitors.

This was not seen for the mixture of BIA + $Ce(NO_3)_3$, in which the addition of the cerium nitrate clearly worsened the inhibition properties in relation to the BIA. This hints at the selectivity and additional effects of the inhibitors used. In this particular case the signs pointing to the reaction between the inhibitors was observed.

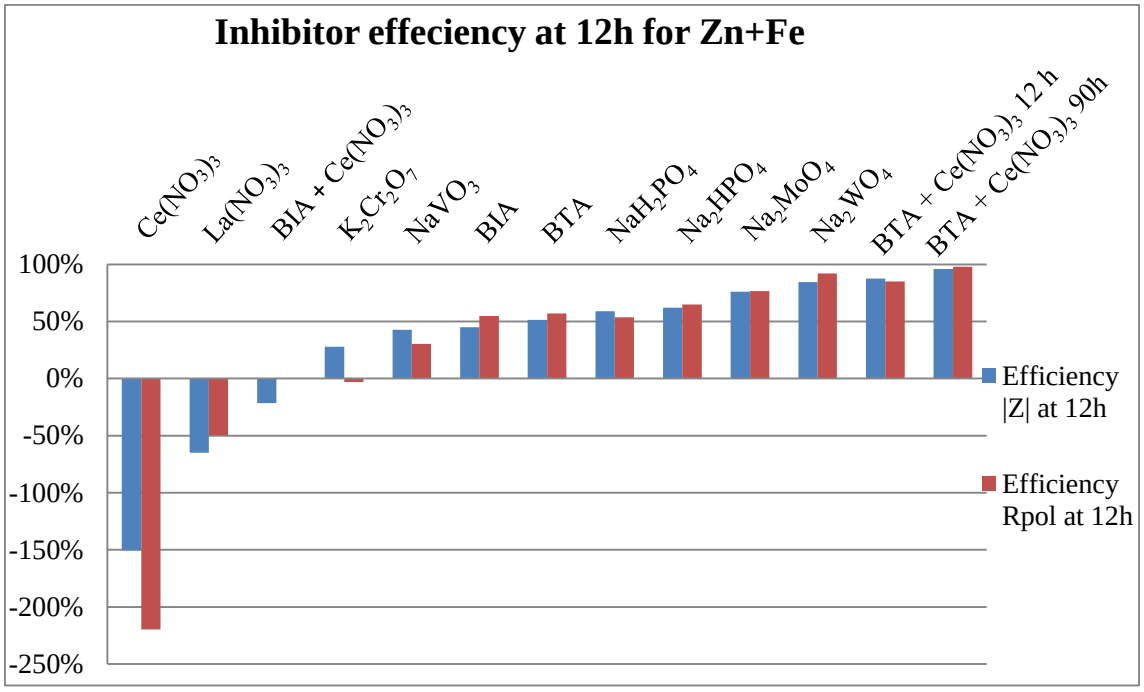

Figure 39. Inhibitor efficiency's calculated from EIS data for the Fe-Zn couple systems at 12h of immersion..

By using Equation 4 we can calculate the synergistic parameter (S). This was done for The BIA and BTA mixtures with Ce^{3+} , as it can be seen in Figure 40.

Previous work with BTA + $Ce(NO_3)_3$ at similar conditions showed a S parameter of 6.091 [4] which is quite close to what was found in this work.

And as expected the S parameter for the BIA containing mixture is very low.

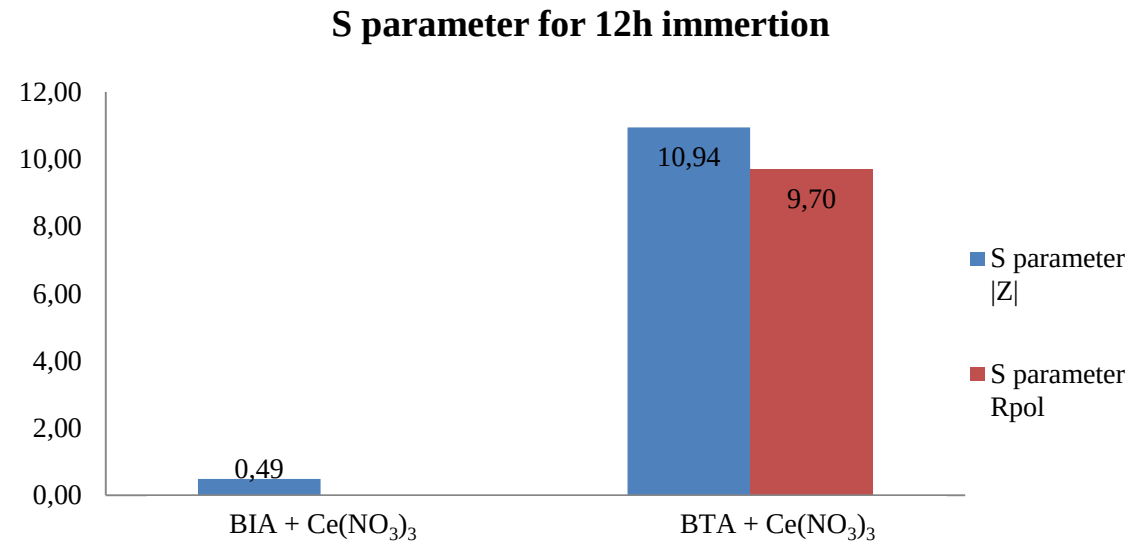

Figure 40. Synergistic parameter calculated with Equation 4, for the BIA + $Ce(NO_3)_3$ and BTA + $Ce(NO_3)_3$, on Zn+Fe galvanic couple substrate.

3.2. Galvanic corrosion study on AA2024 and CFRP couple.

Bare AA2024 samples were measured at steady state conditions (OCP) in various inhibitor systems. Then they were compared with the coupled galvanic cell (GC) and artificially polarized Al alloy (AP) samples.

Conductivity and pH of each solution has been also routinely measured for solutions prepared just for these measurements. The values are presented in Table 7.

Table 7. pH and conductivity values for the used systems

	pH	Conductivity mS/cm
NaCl [50mM]	5,16	5,59
NaCl [50mM] + Na_2WO_4 [5mM]	6,9	6,71
NaCl [50mM] + $NaVO_3$ [5mM]	6,46	5,8
NaCl [50mM] + BTA [5mM]	5,61	5,61
NaCl [50mM] + BIA [5mM]	7,35	5,67
NaCl [50mM] + BTA [2,5mM]+ $Ce(NO_3)_3$ [2,5mM]	4,89	6,22

3.2.1. EIS measurements at OCP

In Figure 41 the surface images of immersed samples after 48 hours are presented. Samples a) and b) show the normal corrosion on unclad AA-2024 in a 50mM Cl^- solution at OCP. A brown discoloration with localized pitting sites is spread throughout the surface.

Sample c) shows situation when the $NaVO_3$ inhibitor has been used. This left a yellow powder which might be a vanadium oxide or hydroxide settled on the pitting sites. Given the short time period the powder must be the hydroxide form.

In sample d) the corrosion in the presence of the Na_2WO_4 in solution can be seen. This inhibitor seems to create a dark brown coating over the aluminium, broken by the pitting sites, obviously in the areas where bigger than average inclusions are present.

Sample e) shows the corrosion in the presence of the BIA. This also causes a discoloration at the surface, but low pitting density on the surface of the sample.

Sample f) and g) show the corrosion in the presence of BTA and BTA + $Ce(NO_3)_3$ respectively, either surface show no visible sign of pitting or any type of corrosion. The

surface of sample g) shows some discoloration but it was due to electrolyte drying on the surface.

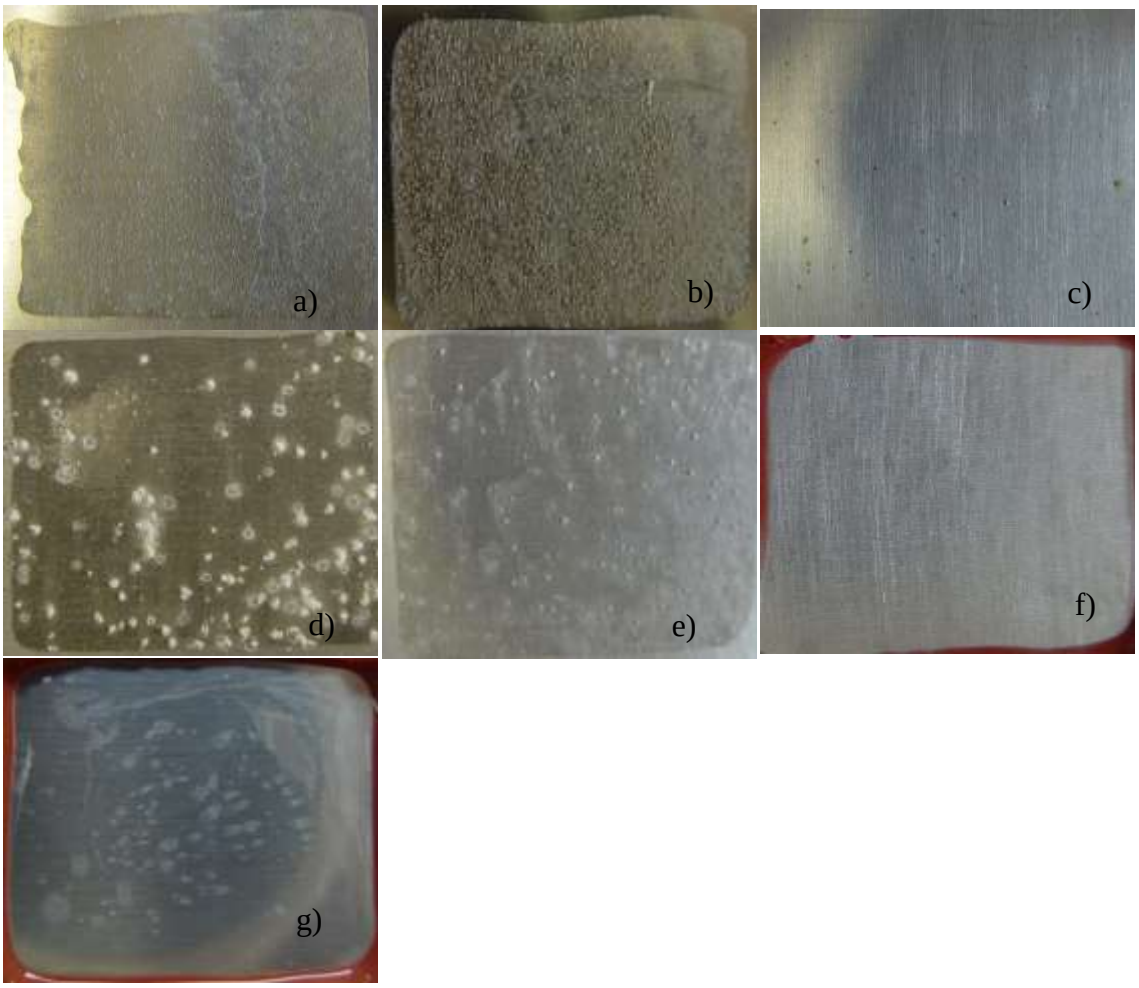

Figure 41. OCP Samples after 48h of immersion in a) NaCl, b) NaCl second, c) $NaVO_3$, d) $NaWO_4$, e) BIA, f) BTA, g) BTA + $Ce(NO_3)_3$.

In Figure 42 the EIS results for all studied systems are presented at the 24h sampling time. The higher impedance of the BTA, BTA + $Ce(NO_3)_3$ and $NaVO_3$ systems in relation to the others is visible. In the theta vs. frequency bode plot, one can see that these three inhibitor systems with higher impedance have one time constant with a very broad peak. The other systems show two time constants, one in the mid frequencies and the other in the low frequencies. In the low frequency part of the spectrum sometimes also the scattering appeared. This has been found to be very common in the case of organic inhibitor systems.

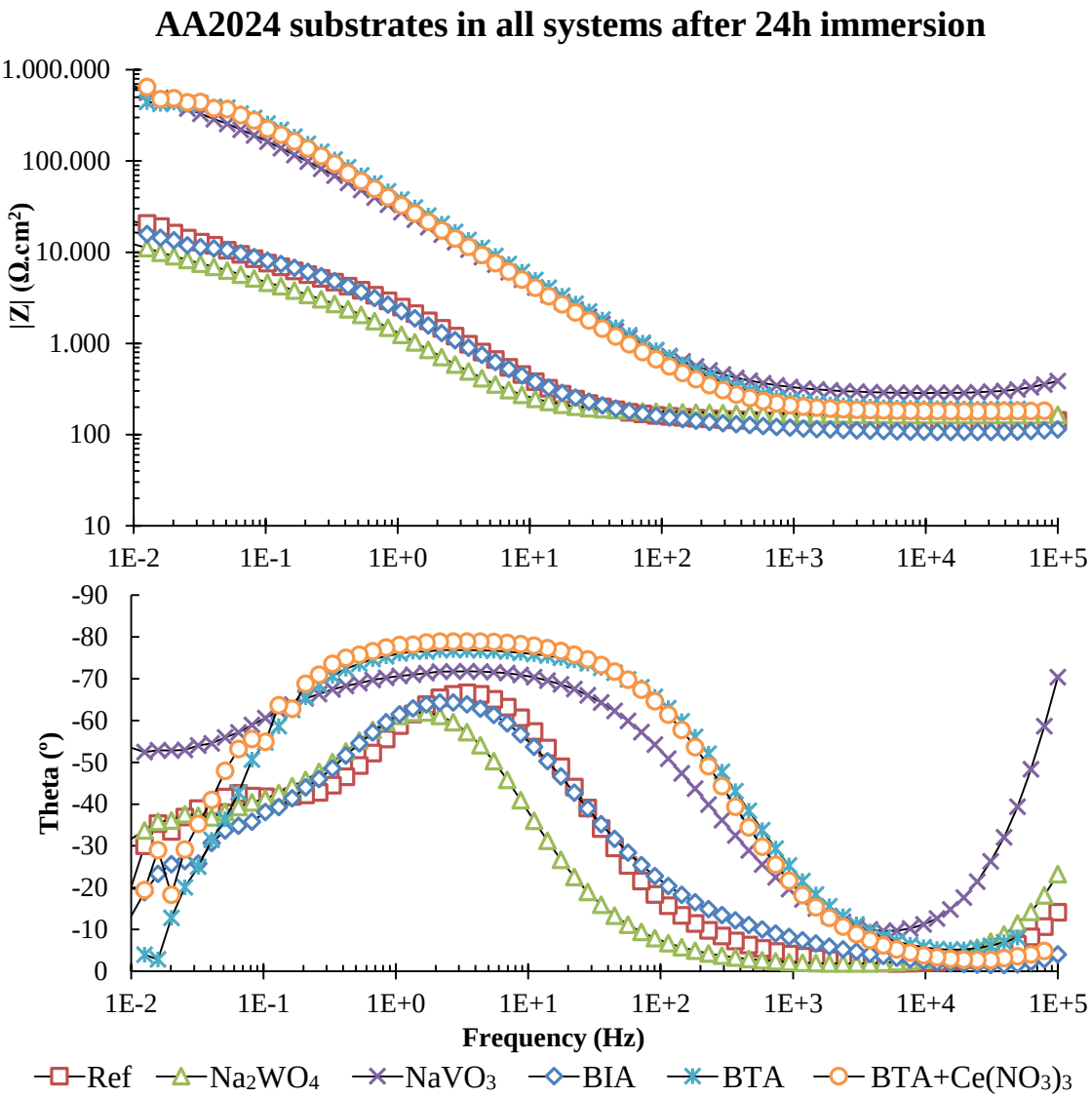

Figure 42. Bode plot of the single Al alloy substrate systems at 24h of immersion.

In Figure 43 the evolution of low frequency impedance at 0.1Hz has been plotted. The frequency was selected due to the observed unwanted scattering of EIS data at lower frequency range.

In the impedance graph of Figure 43 occurs that the BTA, BTA + $Ce(NO_3)_3$ and vanadate systems have a higher impedance than the rest of the systems. This also corresponds to the visual data presented in Figure 41.

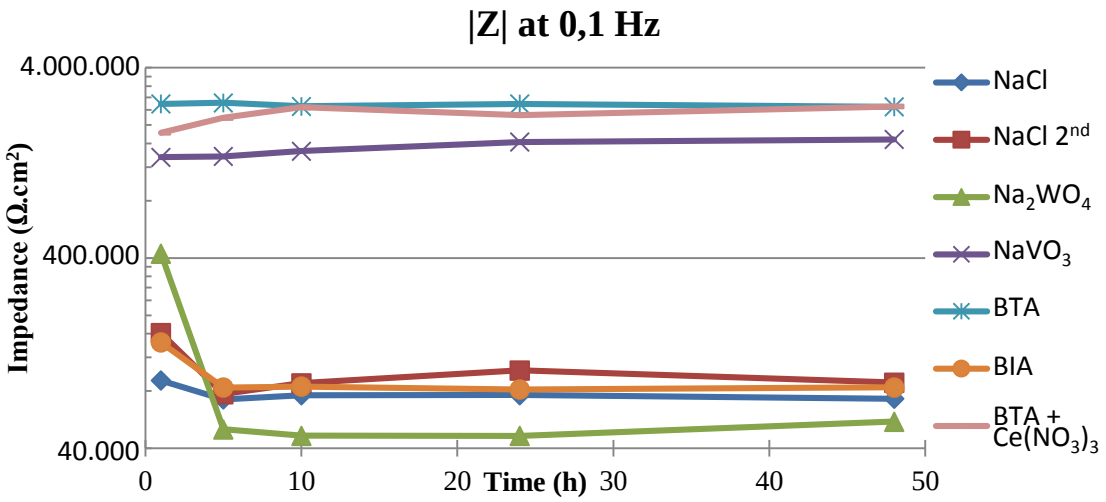

Figure 43. Total impedance in the single Al alloy substrate systems at 0,1 Hz.

For the purpose of deeper analyses of EIS data the spectra were fitted using one and two time constant equivalent circuits presented in Figure 25

In Figure 44 we can see the fitted polarization resistance of the various systems. The polarization resistance is inversely proportional to the corrosion rate and as can be seen the ones that have the higher Rpol are also the systems that show less signs of corrosion.

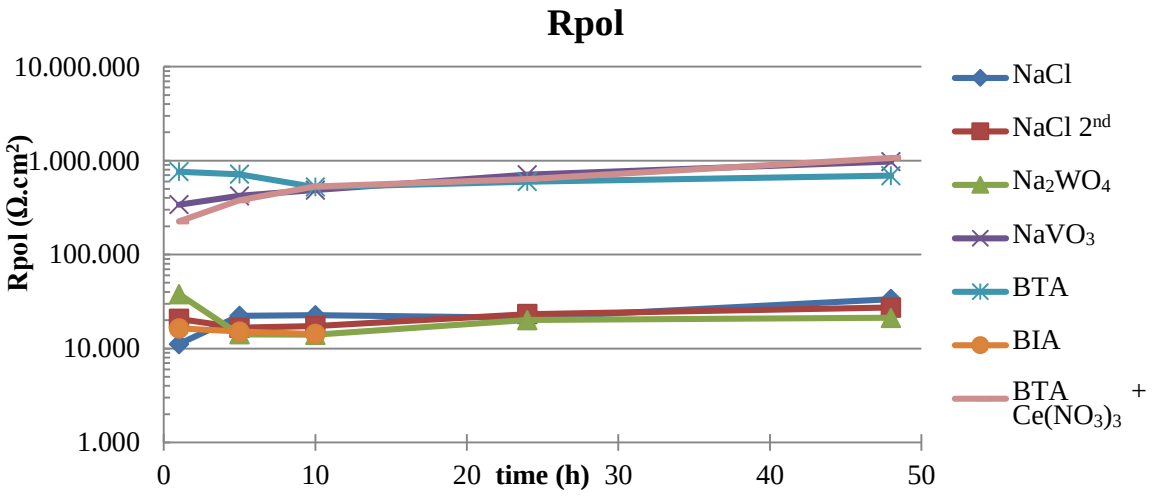

Figure 44. Polarization resistance change over time of the single Al alloy substrate systems.

Using the |Z| and Rpol values and Equation 3, the individual inhibitor efficiencies were calculated and presented in Figure 45. As in the case of both,

the Rpol and |Z|, the difference between the BTA, BTA + $Ce(NO_3)_3$ and $NaVO_3$ and the other systems is greater than one order of magnitude. It is not surprising to find such great inhibitor efficiencies for these inhibitors. However, on the other hand BIA and Na_2WO_4 show only the values which are even below the NaCl reference, giving the negative inhibition efficiency (*IE*) values in the Figure 45.

The EIS spectra for BIA system was only fitted at the 10h time of immersion, because the spectra obtained at 24h and 48 were did not fit sufficiently with selected approach.

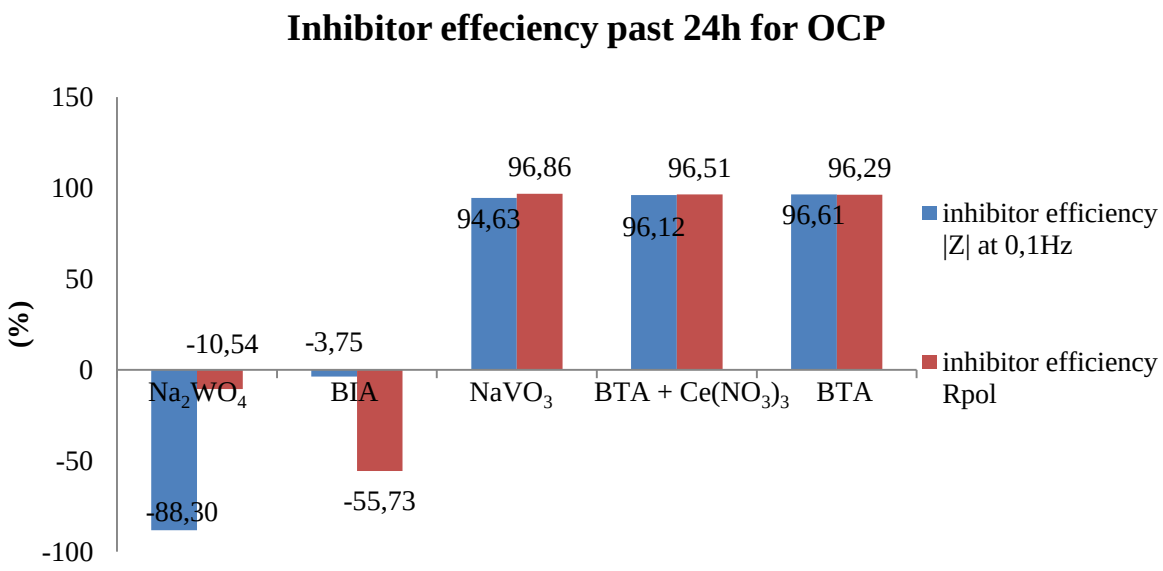

Figure 45. Inhibitor efficiencies for the single Al alloy substrate systems using the 24h data from Rpol and |Z| at 0,1Hz

3.2.2. Galvanically Coupled (GC) and Artificially polarized (AP) systems

Using the same methodologies as in the OCP measurements the Al alloy samples were electrically coupled with CFRP samples forming the model galvanic system.

ZRA was used to measure the current passing between the two electrodes, which would be proportional to the corrosion rate.

In the second stage the Al alloy samples were artificially polarized galvanostatically up to the currents measured previously by ZRA in order to try and simulate the Al alloy response separately in order to emulate the situation where it is in a galvanically coupled system.

Two approaches were used for the artificial polarization. First a potentiostatic polarization using the average potential measured in the ZRA analysis. This approach resulted with significantly higher corrosion rates than the natural galvanically coupled system. Later a galvanostatic artificial polarization approach was tried and this showed more similar results to the natural galvanic couple.

The reason proposed is that the potential of the couple depends on the pitting potential of the Al alloy which is then depending on the activity and number of these sites. As we polarize potentiostatically we might over-polarize the Al alloy sample. When using the galvanostatic polarization approach we force the corrosion rate to stay strictly the same as in the natural couple measured by ZRA.

This can be seen in Figure 46, when comparing the GC Na_2WO_4 system (d) and (e), with the galvanostatically AP and the potentiostatically AP (d') and (e') respectively.

Later EIS data from the AP (bare AA2024) and GC (bare CFRP-AA2024) systems were compared on the basis of the potentials measured during the ZRA in the GC and potential during the polarization in the AP.

Photos of the samples were taken and compared. In Figure 46 we can see all the measured samples. (a) and (b) show coupled samples when exposed just to 50mM NaCl for 48h and were used to determine a reference.

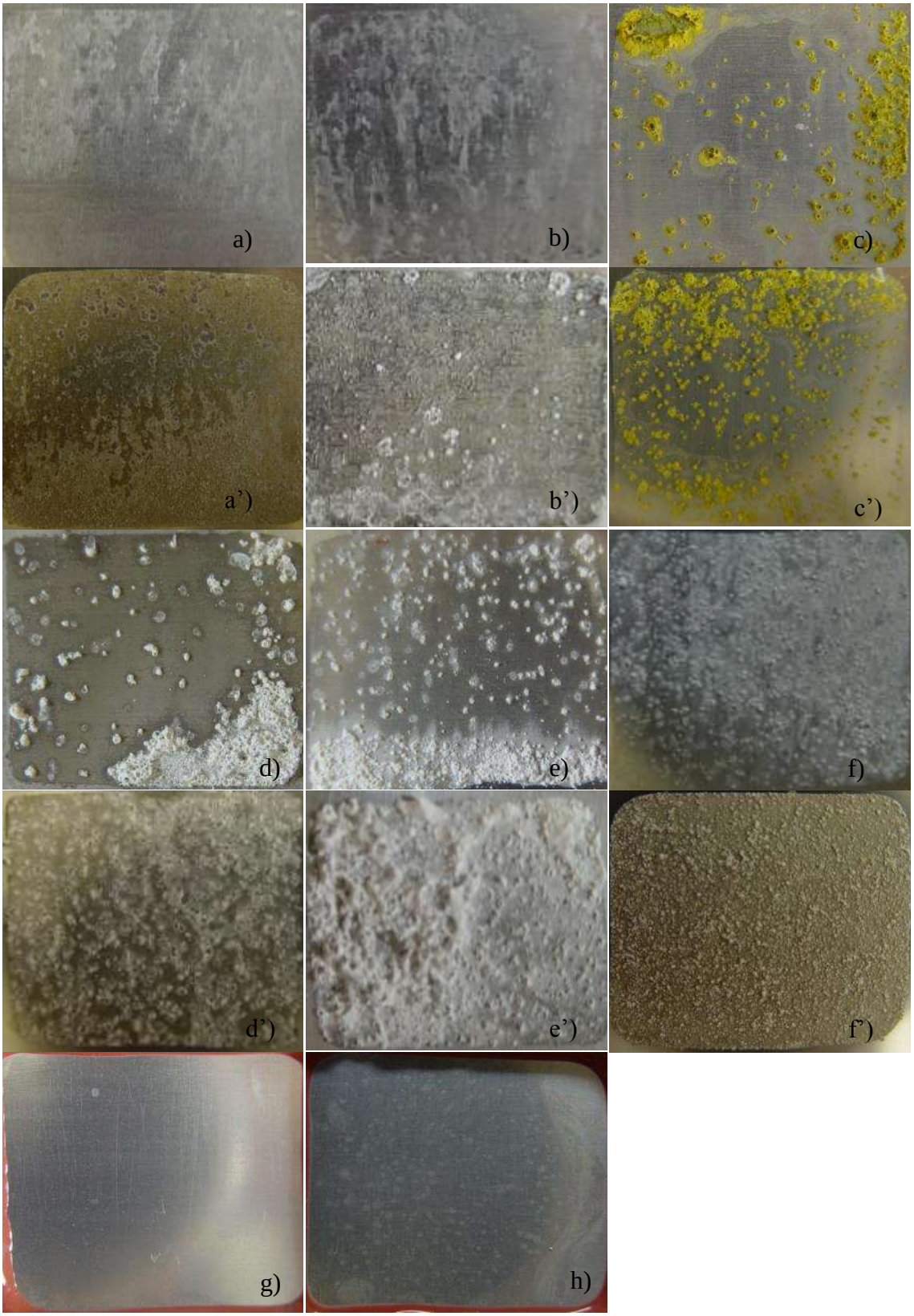
a)
b)
c)
a')
b')
c')
d)
e)
f)
d')
e')
f')
g)
h)

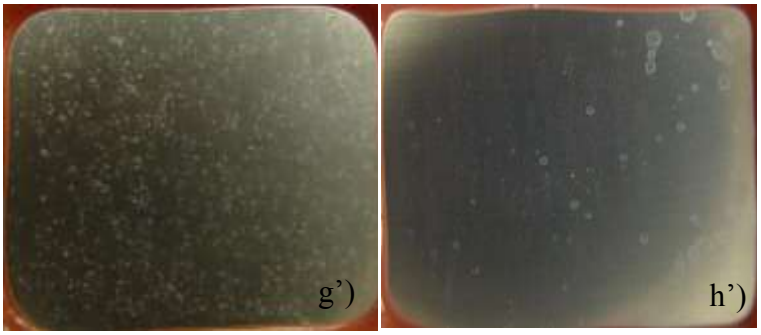

Figure 46. Galvanically coupled samples and artificially polarized samples after 48h immersion, a) NaCl coupled sample, a') NaCl after potentiostatic polarization, b) NaCl coupled sample second time, b') NaCl after galvanostatic polarization, c) $NaVO_3$ coupled sample, c') $NaVO_3$ after galvanostatic polarization, d) $NaWO_4$ coupled sample, d') $NaWO_4$ after galvanostatic polarization, e) $NaWO_4$ coupled sample second time, e') $NaWO_4$ after potentiostatic polarization, f) BIA coupled sample, f') BIA after galvanostatic polarization, g) BTA coupled sample, g') BTA after galvanostatic polarization, h) BTA + $Ce(NO_3)_3$ coupled sample, h') BTA + $Ce(NO_3)_3$ after galvanostatic polarization.

As can be seen, the $NaVO_3$ systems, c) and c'), show the yellow coloring that was also seen in the OCP systems (Figure 41 c). One thing seen across the AP systems is that the corrosion sites seem to be more homogeneously distributed. This is most visible when comparing the GC systems of Na_2WO_4 and $NaVO_3$, d) and e) with the AP d') and e').

The BTA system shows very fine pitting distributed over the entire sample as can be seen in h). In the case of polarized system there is less pitting but with more intensive activities.

In the BTA + $Ce(NO_3)_3$ system one can see some white stains present in the surface. These appeared only after the electrolyte drying. So they could be from the electrolyte solution, or it might be alumina suspended in the solution resulting from corrosion.

ZRA measurements were performed in order to measure the currents going between the AA-2024 and the CFRP over the time, when these are electrically linked. This data can be used to know the relative corrosion rates in various systems and allows to compare them.

In Figure 47 the plot of galvanic current and couple cell potential are shown. In red the current data (mA/cm^2) and in blue the potential (mV vs. SCE). The reference system of 50mM NaCl solution is presented. For the calculations of mean current (green) and mean potential (purple) the earlier sampling times were excluded and only later ones

were used in order to exclude initial instabilities and fluctuations of measurements of measurements.

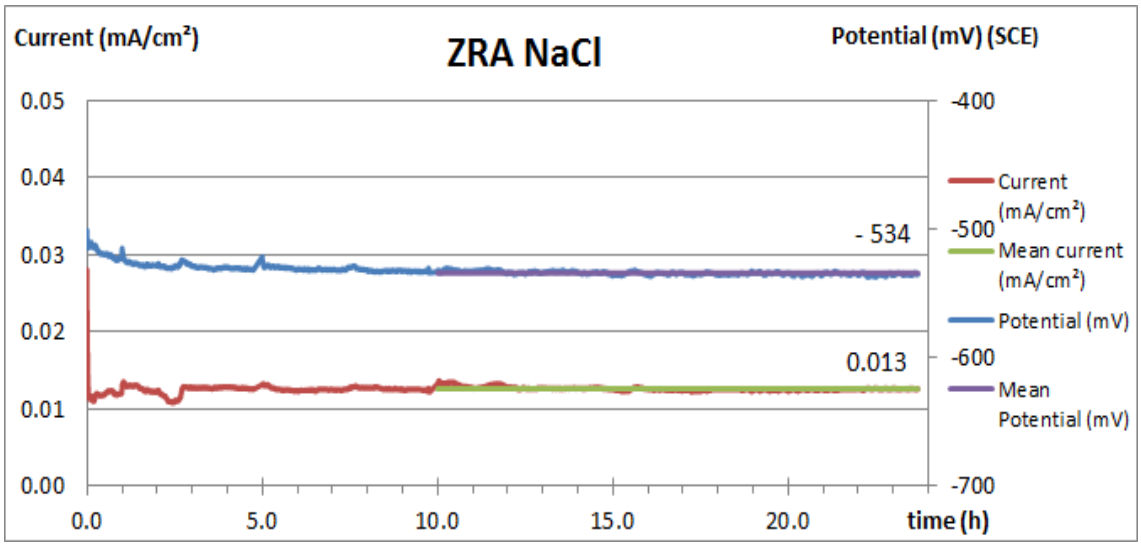

Figure 47. ZRA graph of the coupled system CFRP-AA2024 in NaCl

By compiling this data Table 8 was prepared where the measured currents are presented, as well as the cell-potentials measured in the GC systems and in the galvanostatic AP systems.

It is also important to remark that this data has no statistic relevance as only one sample from each system was done. Also sample areas were very small so the resulting current was small and making small differences in current have big impacts in the later inhibition efficiency calculations.

As it can be expected, the reference system is the one with the highest current. It is also worth to mention, that the combination inhibitor system (BTA + $Ce(NO_3)_3$) shows clearly the lowest galvanic current value.

By comparing both the potential measured in the GC and the AP systems, it follows that these never deviate a lot. This supports the fact that these two systems are similar. Of course further analysis would be need to determine the veracity of this claim.

Table 8. Current measured in the ZRA and potential comparison between coupled system and artificially polarized system.

	$I_{measured}$ (mA/cm^2)	E_{GC} (mV vs. SCE)	E_{AP} (mV vs. SCE)
NaCl (mean)	0,013 0,013 to 0,010	-526 -534 to -518	-544
$NaWO_4$ (mean)	0,011 0,011 to 0,010	-521 -520 to -522	-523
$NaVO_3$	0,007	-518	-545
BTA	0,008	-543	-545
BIA	0,012	-543	-547
BTA + $Ce(NO_3)_3$	0,004	-490	-498

Figure 48 and Figure 49 show the Bode plots from EIS for GC and AP systems at 24h for all inhibitors.

As the galvanic cells are more complicated systems for EIS, the observed spectra also contains more hardly interpretable time constants. Therefore the fitting is also more complicated.

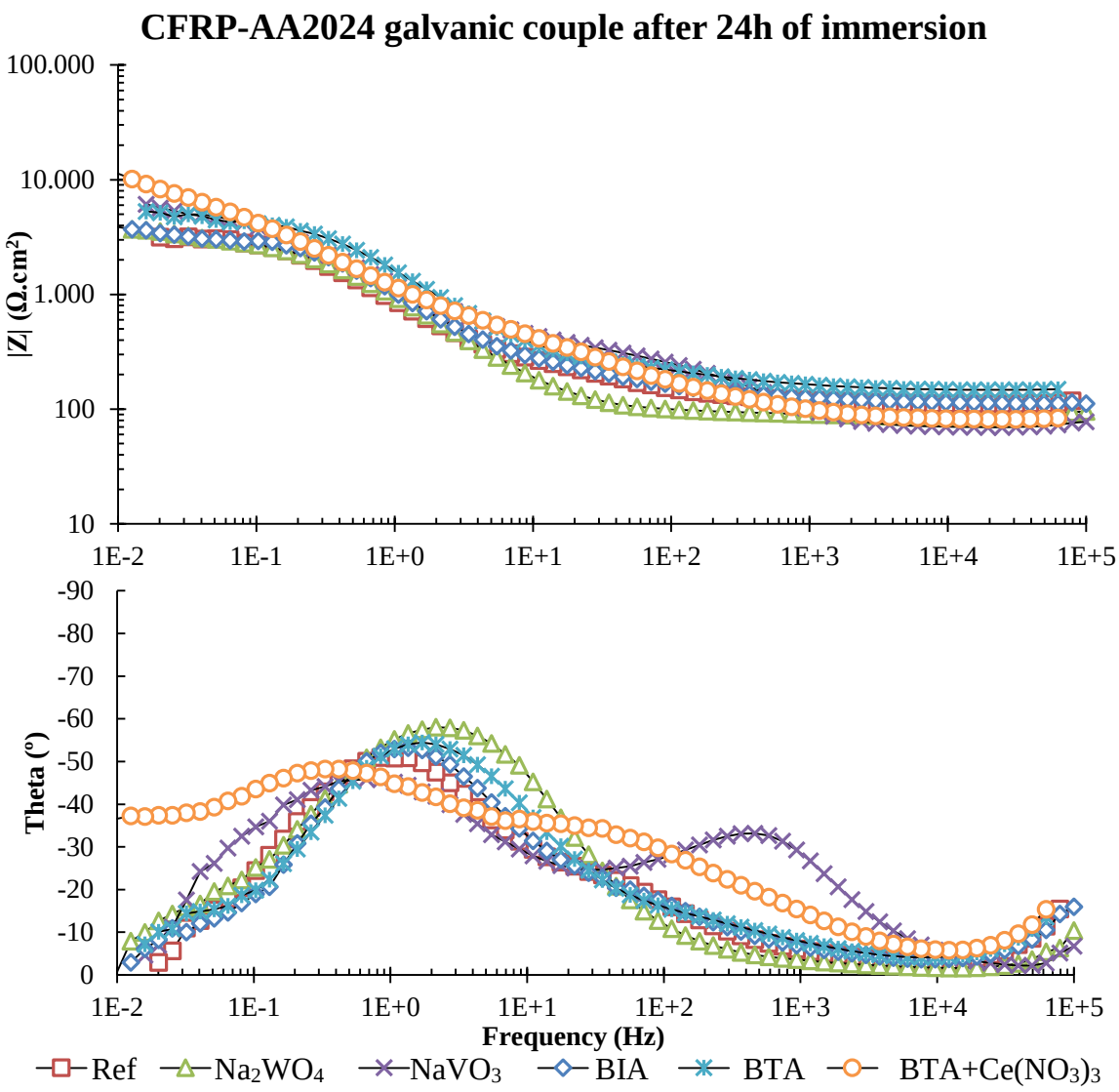

Figure 48. Bode plots of the galvanically coupled system CFRP-AA2024 after 24h of immersion.

In the low frequency range the response is usually due to the electrochemical reactions. These concur with the ZRA data to some extent. In Figure 52 the fitted results of the polarization resistance are plotted and one can see that the systems with higher impedance corresponds to the lower currents measured in the ZRA.

Figure 49 shows the bode plots from the artificially polarized systems at the 24h immersion. The impedance profiles are quite dissimilar, especially in terms of capacitance response in mid frequency range of spectra.

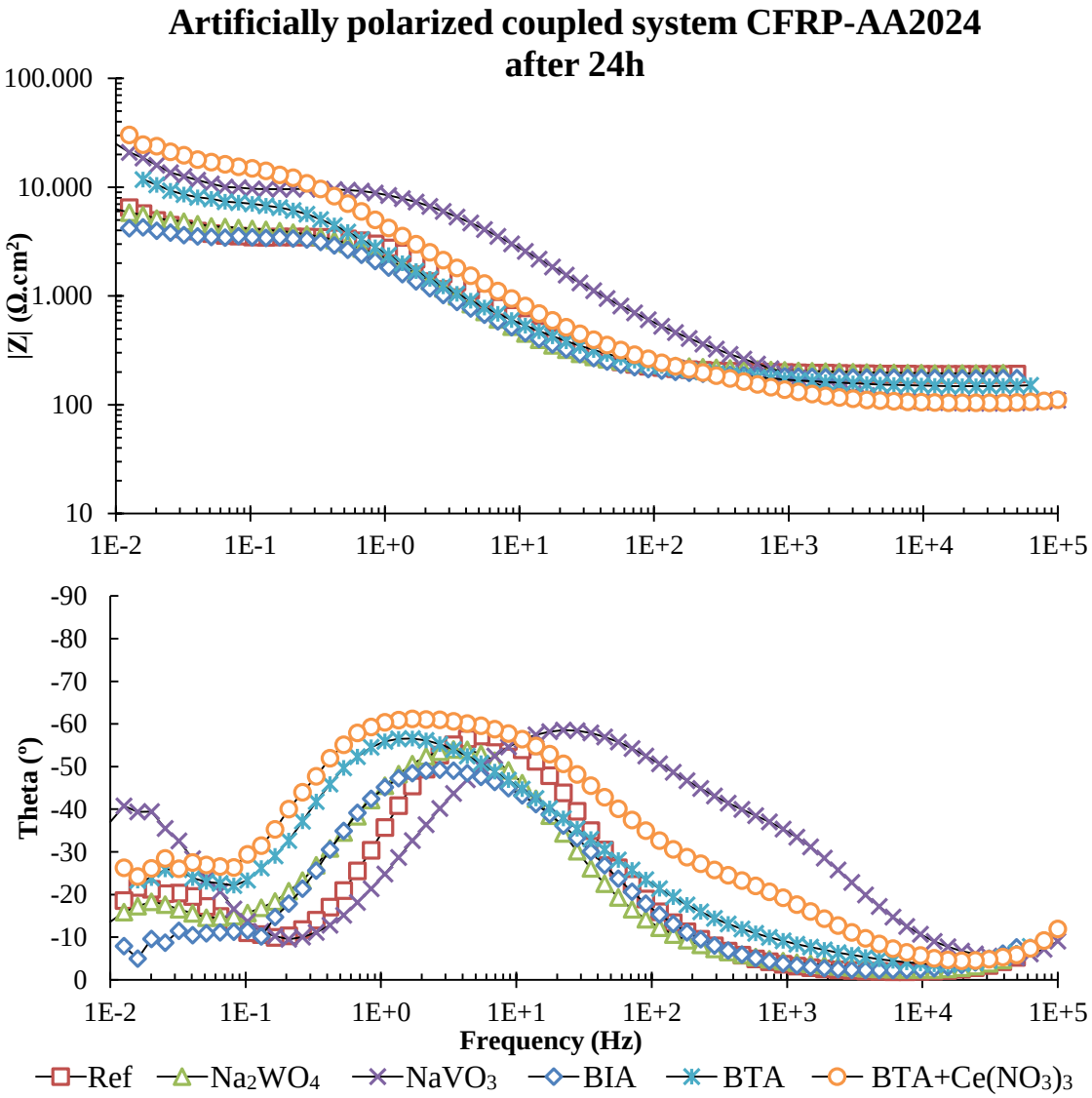

Figure 49. Bode plots of the artificially polarized coupled system CFRP-AA2024 after 24h of immersion.

In the BTA + $Ce(NO_3)_3$ we can see 3 time constants appearing in the high and mid frequencies range. This particular system is quite complex as two inhibitors with different mechanisms are being used simultaneously.

One thing that is common over all the AP systems is the time constant that appears at the very low frequencies. This seems to grow as time goes by and it was attributed to oxygen deficiency in the electrolyte solution. The influence of that low frequency time constant was avoided during the fittings, as it inflated the polarization resistance giving unreliable values.

In Figure 50 one can see the evolution of total impedance of the GC systems at 0,1 Hz and this correlates with the ZRA data in some points. This graph takes in to account data from 0,1Hz, which is not the lowest frequency sampled. The frequency 0,01 Hz would be also good comparison for corrosion understanding as the electrochemical reactions take place near those frequencies. But data analysis at these frequencies becomes hard due to the occurrence of scattering of the data points.

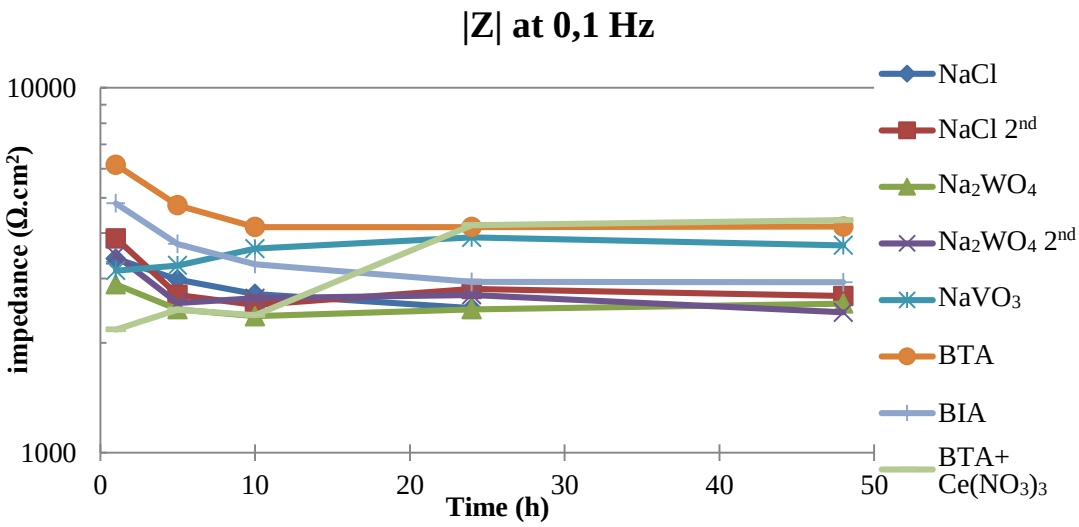

Figure 50. Total impedance in the galvanically coupled CFRP-AA2024 systems at 0,1 Hz.

The same EIS data was collected and treated for the AP AA2024 samples. As it can be seen in Figure 51, although the relation in impedance between each inhibitor is the same, the impedance profile of each inhibitor is different when compared with Figure 50. Here the combination inhibitor system BTA + $Ce(NO_3)_3$ prevails over the rest of the systems.

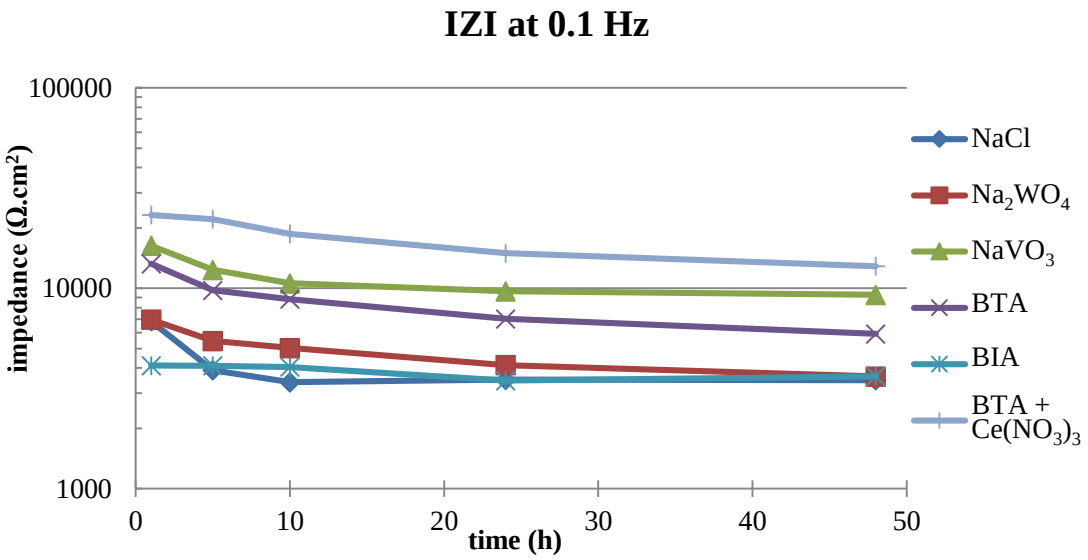

Figure 51. Total impedance in the artificially polarized coupled system CFRP-AA2024 at 0,1 Hz.

By fitting the EIS data with the equivalent circuits shown in Figure 25 the fitting of the Rpol of the GC and AP systems can be done as it was done for the OCP systems.

In Figure 52 the fitted values of Rpol for the GC system are presented. They concur generally with the ZRA measurements as BTA + $Ce(NO_3)_3$, $NaVO_3$ and BTA are above the others. Especial emphasis must be given to the synergetic mixture BTA + $Ce(NO_3)_3$ which shows clear superiority over the others.

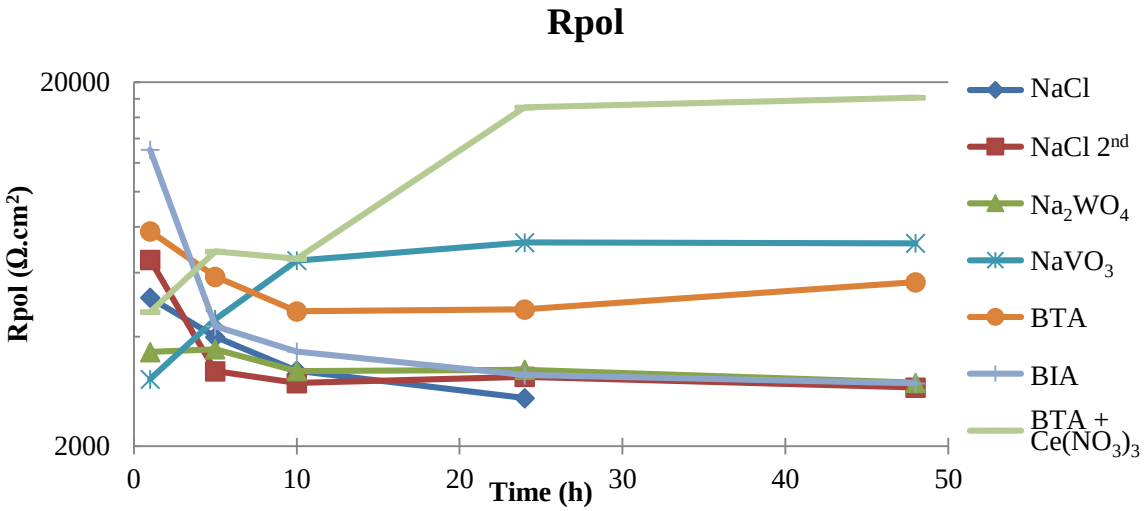

Figure 52. Polarization resistance change over time of the galvanically coupled CFRP-AA2024 systems.

Figure 53 shows the detailed analysis of the inhibitor mixture over the 24h analysis in the GC system.

As it can be seen, the |Z| rises slightly with the time and the system seems to become more capacitive with time. This would occur if a protecting ad-layer was forming at the surface and getting thicker with time. This is supported by the phase angle displacement during the time.

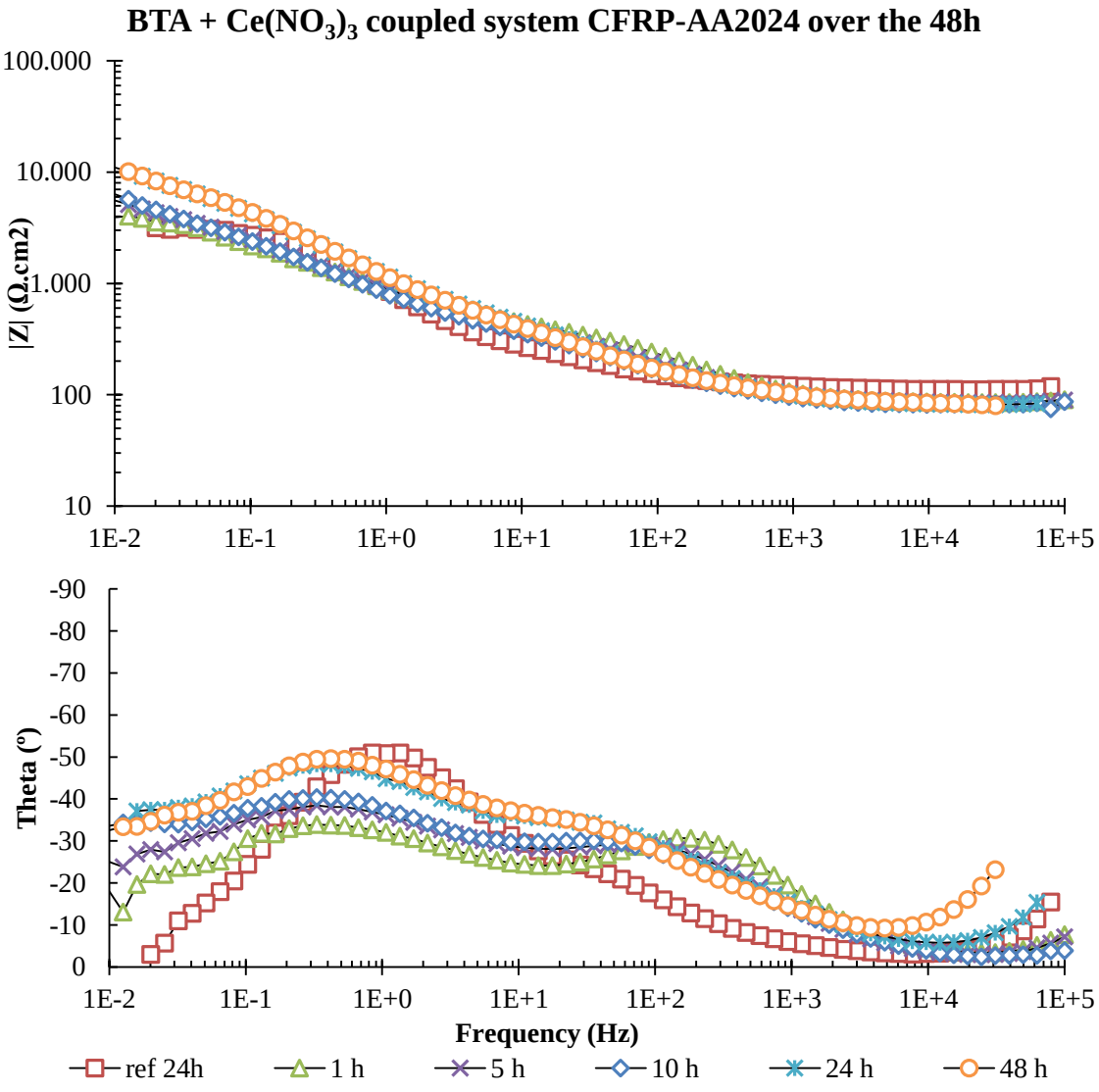

Figure 53. Bode plots for the BTA + $Ce(NO_3)_3$ coupled system CFRP-AA2024 over the 48h measurement.

In Figure 54 we can see the evolution of fitted Rpol. for artificially polarized systems.

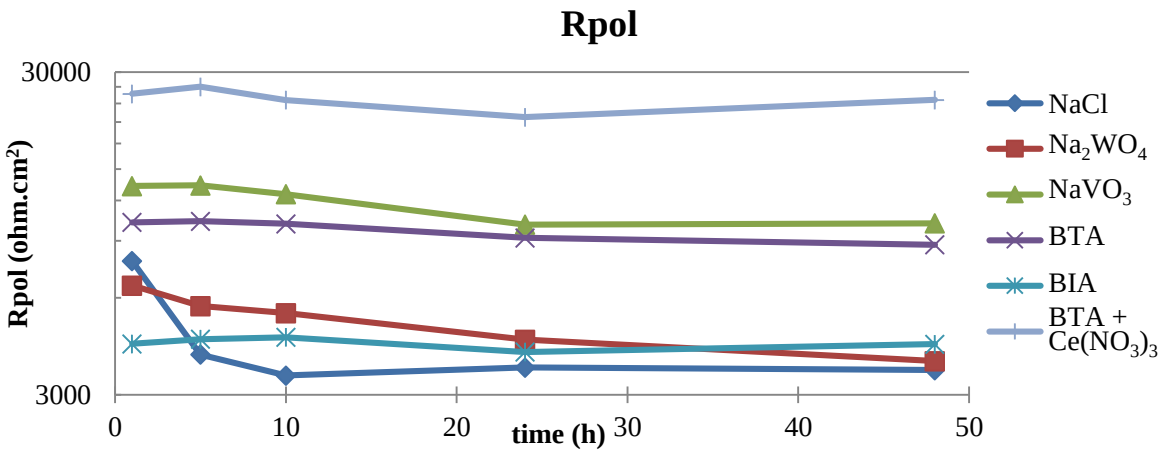

Figure 54. Polarization resistance evolution over time of the artificially polarized coupled CFRP-AA2024 system.

By analyzing the data compiled in Table 8 and using Equation 2 the inhibition efficiency of the inhibitors used can be calculated. Figure 55 shows the inhibitor efficiency relative to the mean current calculated from the reference samples. One can see that the BTA + $Ce(NO_3)_3$ shows a very good effect, which correlates with the sample photo i) in Figure 46 and all the EIS data.

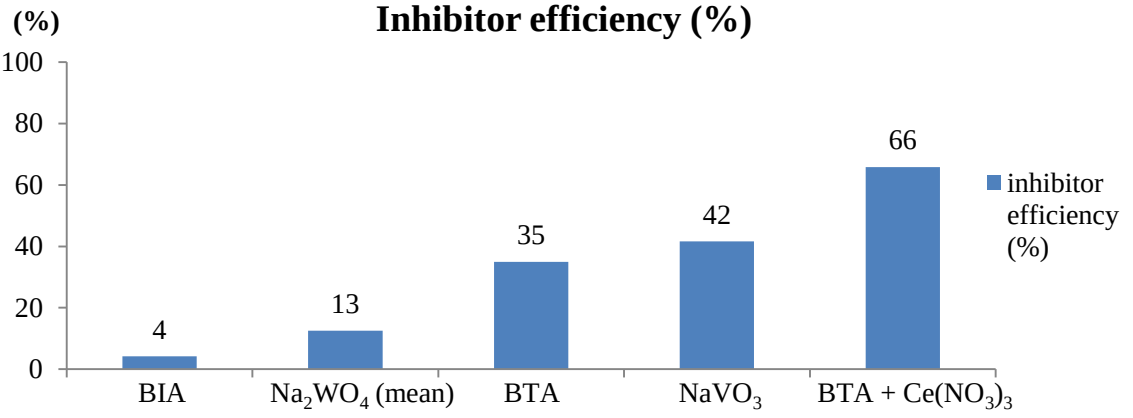

Figure 55. Inhibitor efficiency calculated with ZRA data for the coupled CFRP-AA2024 system.

As Rpol and |Z| are inversely proportional to the corrosion rate, by comparing each inhibitor containing system to the non-inhibited, one can calculate the inhibition

efficiency, using a variation of Equation 2 in which the current intensity is substituted by corrosion rate.

In Figure 56 the inhibitor efficiency of the GC systems are plotted. These graphs make it easier to compare to the qualitative results of the EIS measurements with the ZRA ones shown in Figure 55. As can be seen, they match up very well in qualitative terms.

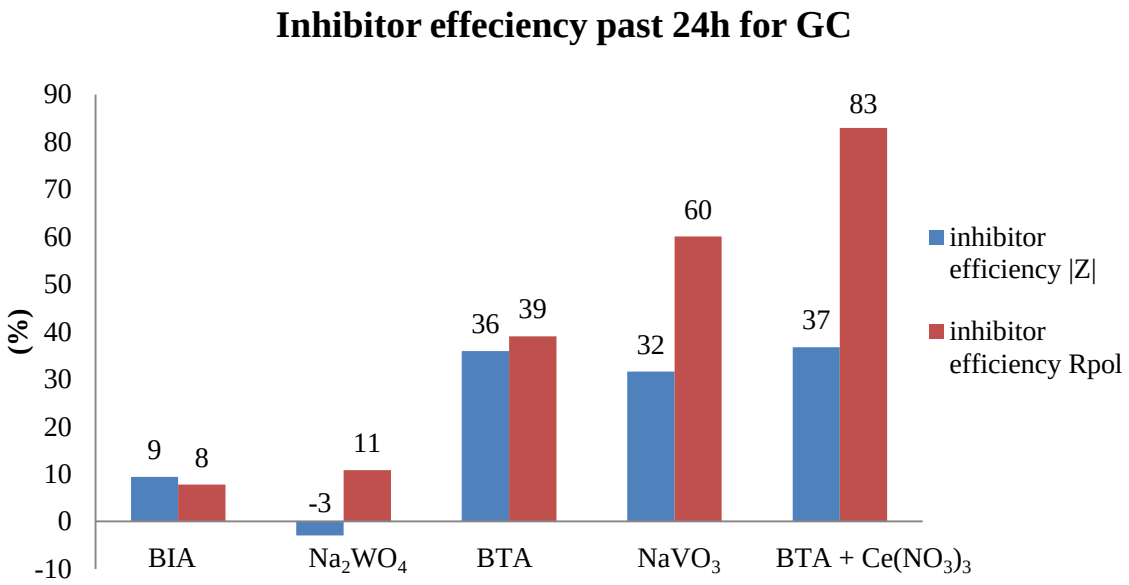

Figure 56. Inhibitor efficiency calculated with EIS data for the coupled CFRP-AA2024 system.

In Figure 57 one can see the inhibition efficiency of the AP systems calculated using the EIS data. The striking similarities between the GC and AP are visible which strengthens the belief that galvanostatic AP of Al alloy gives a good simulation of galvanic coupling at least for AA-2024 in sodium chloride solution.

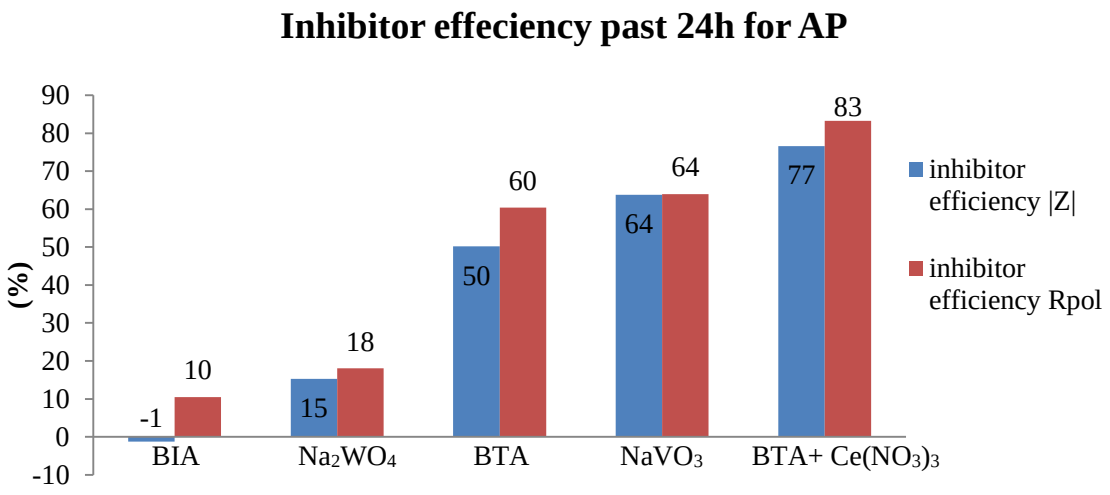

Figure 57. Inhibitor efficiency calculated with EIS data for the AP coupled CFRP-AA2024 system.

4. Conclusions

A selection of corrosion inhibitors were tested in different conditions in iron, zinc and AA2024 single electrode substrate as well as on Fe + Zn and AA2024 + CFRP galvanically linked electrode substrates.

Systematic analyzes with conventional electrochemical techniques such as EIS and ZRA were done for evaluation of corrosion properties of galvanic and single electrode systems.

The EIS measurements on galvanic pairs and for single electrode substrates showed that there was a definite change in the impedance response of the systems. Contrary to the possibility that only the least resistive substrate would influence the response.

It has found that the tested potentially synergetic mixture of inhibitors (BTA + $Ce(NO_3)_3$) has been performing better than the rest, especially with the cases of galvanic corrosion. Even though the advantage was not clearly distinct on steady state (OCP) corrosion conditions at AA2024, the performance at more complicated galvanic corrosion circumstances seems to be promising. This also correlates to the recently observed lab-scale behavior of this inhibitor mixture that was observed with more localized electrochemical techniques.

In case of the Zn-Fe galvanic pair the BTA is supposed to adsorb specifically on the zinc surface and the precipitated $Ce(OH)_3$ acts as a cathodic blocker at the iron surface, which is accordance with the previous knowledge based on the literature.

Also in case of the AA2024-CFRP pair there is a strong inhibition effect. The $Ce(NO_3)_3$ also forms precipitates on the cathodic sites, while differently from ZN-Fe system the BTA contributes on the copper rich intermetallic on the anode side (AA2024) decreasing its activities significantly.

Also the potentiostatic and galvanostatic simulation of galvanic couple conditions to the AA2024 has been tested. It occurs, that the galvanostatic simulation based on natural couple cell current has been more successful.

Novel approaches to galvanic system studies, must be further developed. A better understanding of the EIS on more complicated galvanic systems as well as the more systematic and supportive usage of localized electrochemical techniques will be the goal for future developments.

5. References

1. *Screening of corrosion inhibitors for galvanic systems by SVET, using multi-electrode model arrays.* **S. Kallip, A.C. Bastos, M.L. Zheludkevich, M.G.S. Ferreira.** Salt Lake City : s.n., 2012. NACE - International Corrosion Conference Series: Corrosion 2012. Vol. 7, pp. 5333 - 5339.

2. **S. Palani, T. Hack, J. Deconinck, H. Lohner.** Validation of predictive model for galvanic corrosion under thin electrolyte layers: An application to aluminium 2024-CFRP material combination. *Corrosion Science.* 2014, Vol. 78, pp. 89-100.

3. **corrosionist. [Online] http://www.corrosionist.com/.**

4. S. Kallip, A. C. Bastos, K. A. Yasakau, M. L. Zheludkevich, M. G.S. Ferreira. Synergistic corrosion inhibition on galvanically coupled metallic materials. *Electrochemistry Communications.* 2012, Vol. 20, pp. 101-104.

5. A.M. Simões, A.C. Bastos, M.G. Ferreira,Y. González-Garcıá, S. González, R.M. Souto. Use of SVET and SECM to study the galvanic corrosion of an iron–zinc cell. *Corrosion Science.* 2007, Vol. 49, pp. 726–739.

6. E. A. Starke Jr, J. T. Staley. Application of modern aluminium alloys to aircraft. *Pro 9. Aerospace Sci.* 1996, Vol. 32, pp. 131-172.

7. L. Lacroix, C. Blanc, N. Pébère, G.E. Thompson, B. Tribollet, V. Vivier. Simulating the galvanic coupling between S-Al2CuMg phase particles and the matrix of 2024 aerospace aluminium alloy. *Corrosion Science.* 2012, Vol. 64 , pp. 213–221.

8. Z. Peng, X. Nie. Galvanic corrosion property of contacts between carbon fiber cloth materials and typical metal alloys in an aggressive environment. *Surface & Coatings Technology.* 2013, Vol. 215 , pp. 85–89.

9. aluMATTER.[Online] http://aluminium.matter.org.uk/content/html/eng/default.asp?catid=180&pageid=2144416698.

10. S.R. Karnik, V.N. Gaitonde, J. C. Rubio, A. E. Correia, A.M. Abrão, J. P. Davim. Delamination analysis in high speed drilling of carbon fiber reinforced plastics

(CFRP) using artificial neural network model. *Materials and Design.* 2008, Vol. 29, pp. 1768–1776.

11. K.-H. Tytko, O. Glemser. Isopolymolybdates and Isopolytungstates. *Advances in Inorganic Chemistry and Radiochemistry.* 1976, Vol. 19, pp. 239–315.

12. M.I. Borzenko, G.N. Botukhova, G.A. Tsirlina, O.A. Petrii. Electrochemistry of isopolytungstate mixtures. *Electrochimica Acta.* 2008, Vol. 53, pp. 3854–3861.

13. P. Wang, X. Dong, D. W. Schaefer. Structure and water-barrier properties of vanadate-based corrosion inhibitor films. *Corrosion Science.* 2010, Vol. 52, pp. 943–949.

14. M. Iannuzzi, G.S. Frankel. Mechanisms of corrosion inhibition of AA2024-T3 by vanadates. *Corrosion Science.* 2007, Vol. 49, pp. 2371–2391.

15. A.C. Bastos, M.G. Ferreira, A.M. Simões. Corrosion inhibition by chromate and phosphate extracts for iron substrates studied by EIS and SVET. *Corrosion Science.* 2006, Vol. 48, pp. 1500–1512.

16. J. Zhao, L. Xia, A. Sehgal, D. Lu, R.L. McCreery, G.S. Frankel. Effects of chromate and chromate conversion coatings on corrosion of aluminum alloy 2024-T3. *Surface and Coatings Technology.* 2001, Vol. 140, pp. 51–57**.**

17. J.V. Kloet, W Schmidt, A.W Hassel, M Stratmann. The role of chromate in filiform corrosion inhibition. *Electrochimica Acta.* 2004, Vol. 49, pp. 1675–1685.

18. A. K. Mishra, R. Balasubramaniam. Corrosion inhibition of aluminum alloy AA 2014 by rare earth chlorides. *Corrosion Science.* 2007, Vol. 49, pp. 1027–1044.

19. J. Tedim, A. Kuznetsova, A.N. Salak, F. Montemor, D. Snihirova, M. Pilz, M.L. Zheludkevich. Zn–Al layered double hydroxides as chloride nanotraps in active protective coatings. *Corrosion Science.* 2012, Vol. 55, pp. 1-4.

20. M. Finšgar, I. Milošev. Inhibition of copper corrosion by 1,2,3-benzotriazole: A review. *Corrosion Science.* 2010, Vol. 52, pp. 2737–2749.

21. corrosionservice. Zero Resistance Ammeter (ZRA). *Corrosion Service.* [Online] corrosionservice, 2012. http://www.corrosionservice.com/zero_resistance_ammeter.htm.

22. B. Yevgen, J. R. Macdonald. Electroquemichal impedance technique. *Characterization of Materials.* s.l. : John Wiley & Sons, Inc., 2012.

23. A. C. Bastos, S. A. S. Dias, T. C. Diamantino, M. G. S. Ferreira. Uma introdução à técnica SVET. *Corros. Prot. Mater.* 2013, Vol. 32, pp. 50-57.

24. K. Aramaki, N. Hackerman. *Journal of the Electrochemical Society.* 1969, Vol. 116, p. 568.

25. S. Mamas, T. Kıyak, M. Kabasakaloglu, A. Koc. The effect of benzotriazole on brass corrosion. *Materials Chemistry and Physics.* 2005, Vol. 93, pp. 41–47.

26. T. Kosec, I. Milošev, B. Pihlar. Benzotriazole as an inhibitor of brass corrosion in chloride solution. *Applied Surface Science.* 2007, Vol. 253, pp. 8863–8873.

27. T. Kosec, D. K. Merl, I. Milošev. Impedance and XPS study of benzotriazole films formed on copper, copper–zinc alloys and zinc in chloride solution. *Corrosion Science.* 2008, Vol. 50, pp. 1987–1997.

28. E. Barsoukov, J. R. Macdonald. *Impedance Spectroscopy Theory, Experiment, and Applications.* New Jersey : John Wiley & Sons, Inc., 2005. ISBN: 0-471-64749-7.